Title: Quartz fluid inclusion abundance and off-fault damage in a deeply exhumed, strike-slip, seismogenic fault

Authors: Won Joon Song[a,]*, Scott E. Johnson[a], Christopher C. Gerbi[a]

Affiliations:

[a]School of Earth and Climate Sciences, University of Maine, Orono, Maine 04469, USA

E-mail addresses:

wonjoon.song@maine.edu (W.J. Song)*, johnsons@maine.edu (S.E. Johnson), christopher.gerbi@maine.edu (C.C. Gerbi)

*Corresponding author

Keywords:

Fluid inclusion; fault damage zone; off-fault damage; frictional-to-viscous transition; seismic cycle; quartz

Highlights:

- Quartz records co-seismic damage in a mid-crustal strike-slip fault/shear zone
- Fluid-inclusion abundance shows a low-high-low trend from the shear zone core
- Fluid-inclusion abundance is reduced by post- and inter-seismic recrystallization
- Reduction of fluid-inclusion abundance is greatest in the inner shear zone
- The off-fault damage zone is >~80 m wide at frictional-to-viscous transition depths

Abstract

Off-fault damage zones comprise highly fractured rocks surrounding the dynamic slip surface of faults. These damage zones modify fault-zone rheology and rupture dynamics by changing the bulk elastic properties and modulating fluid flow. Damage zones in the brittle upper crust, reaching widths >100 m, are commonly characterized by measuring fracture density, but identifying the extent of off-fault damage in deeply exhumed faults is challenging due to post- and inter-seismic viscous/plastic deformation. We measured fluid inclusion abundance in quartz deformed at ~400–500 °C from an ancient seismogenic strike-slip fault/shear zone to evaluate whether it can be a proxy for damage-zone width. In contrast to upper crustal fault zones displaying a high-low trend of healed microfracture density, the shear zone has a low-high-low trend of fluid inclusion abundance from the core toward the host rock. We find that pattern explicable through removal of fluid inclusions by recrystallization after co-seismic deformation, allowing us to use fluid inclusion abundance to measure damage zone extent, which is >~80 m (the low-high abundance region) from the shear zone core. Our findings indicate that extensive co-seismic damage zones may extend from Earth's surface to the base of the seismogenic zone, well within the frictional-to-viscous transition.

1. Introduction

Large-displacement strike-slip faults display off-fault damage zones with macro- or microfracture density increasing toward the fault core, and pulverization of specific rock types showing intense fragmentation to submicron scale without obvious shear strain (e.g., Chester et al., 1993; Ben-Zion and Sammis, 2003; Dor et al., 2006; Mitchell and Faulkner, 2009; Rockwell et al., 2009; Mitchell et al., 2011; Savage and Brodsky, 2011; Rempe et al., 2013). Damage zones represent a channel of low seismic-wave velocities caused by reduction in elastic stiffness (e.g., Li et al., 1990; Ben-Zion, 1998; Ben-Zion et al., 2003; Li et al., 2006; Cochran et al., 2009; Huang and Ampuero, 2011). The fractured damage zones affect local stress distributions

(Faulkner et al., 2006) and earthquake rupture dynamics (e.g., Cappa et al., 2014; Huang et al., 2014; Thomas et al., 2017) either promoting supershear earthquakes with ruptures propagating faster than shear waves (e.g., Huang et al., 2016; Perrin et al., 2016), or decreasing rupture velocity (Okubo et al., 2019). They can also enhance high-frequency radiation and near-fault ground motion (Spudich and Olsen, 2001; Huang and Ampuero, 2011; Castro and Ben-Zion, 2013; Okubo et al., 2019). Therefore, the distribution of fault damage zones is important for seismic hazard assessment.

During a major earthquake in continental crust, co-seismic rupture nucleated in the brittle seismogenic zone can propagate down into rocks that deform viscously in inter-seismic periods (Fig. 1; e.g., Sibson, 1977; Tse and Rice, 1986; Scholz, 1988; Handy et al., 2007). Such temporal variations between brittle and viscous behavior can be identified in nature, for example, by observation of mutually cross-cutting pseudotachylyte and mylonite (e.g., Handy et al., 2007) or mutually overprinting healed microcracks and subgrains/recrystallized grains (e.g., Hirth and Beeler, 2015).

How deep damage zones extend from the surface is important because damage at depth related to earthquake cycles leads to transient fluid flow and rheological changes (e.g., Handy et al., 2007) by influencing permeability (e.g., Mitchell and Faulkner, 2008; Faulkner et al., 2010), thermal structure (e.g., Morton et al., 2012; Ben-Zion and Sammis, 2013) and grain/particle size (e.g., Chester et al., 2005; Trepmann et al., 2007) within and around the fault/shear zone core. As a result of fluid flow through the damage zone, post-seismic redistribution of pore-fluid pressure can reduce fault strength and trigger aftershocks (Miller et al., 2004). In addition, estimating the 3-D volume of the damage zone is important for estimating the inelastic energy dissipated during rupture, the remaining elastic energy being radiated as seismic waves (e.g., Andrews, 2005; Rice et al., 2005; Kanamori and Rivera, 2006; Shipton et al., 2006; Okubo et al., 2019).

Studies of exhumed faults from the upper 10 km of the continental crust show that damage zones can be hundreds of meters wide (e.g., Mitchell and Faulkner, 2009; Faulkner et al., 2011; Savage and Brodsky, 2011). Seismological studies show possible depth limits (4–15 km deep) of damage zones (e.g., Ben-Zion et al., 2003; Li and Malin, 2008; Cochran et al., 2009; Ben-Zion and Zaliapin, 2019), and numerical modeling suggests that off-fault damage zone width decreases with depth (e.g., Okubo et al., 2019). Studies of exhumed faults/shear zones from middle and lower crustal depths documented the occurrence of off-fault damage and pulverization in thrust (e.g., Jamtveit et al., 2019), normal (e.g., Soda and Okudaira, 2018), and strike-slip (e.g., Sullivan and Peterman, 2017) fault systems, often showing locally varying kinematics. However, there have been few systematic geological studies (e.g., Song et al., 2020) to assess the extent of off-fault damage in strike-slip faults exhumed from frictional-to-viscous transition (FVT) depths. Characterizing the extent of brittle damage in rocks exhumed from such depths, near the base of the seismogenic zone, is difficult because evidence of co-seismic damage (e.g., healed intragranular microcracks) in many minerals (e.g., quartz) is typically erased or altered by crack healing and post- and inter-seismic viscous/plastic deformation. Minerals such as feldspar that undergo brittle deformation at these conditions are also altered by processes such as granular flow of fragments during inter-seismic deformation, making it difficult to parse out the co-seismic contribution to the microstructure.

Several studies attempted to find quartz microfabrics diagnostic of transient co-seismic damage under FVT conditions, where quartz experiences plastic deformation during inter-seismic periods. Novel experiments of non-steady state behavior in quartz to simulate the co- and post-seismic deformation in the middle crust (Trepmann et al., 2007) and natural rock studies compared to it (e.g., Trepmann et al., 2017) provided, as evidence for transient co-seismic damage, (a) narrow zones of fine recrystallized grains cutting through parent quartz grains, (b) large misorientation angle between parent and recrystallized grains, and/or (c) random or preferred crystallographic orientation of recrystallized grains depending on post-seismic stress relaxation rates, in addition to direct observation of healed microcracks by transmission electron microscopy, although large misorientations between parent and recrystallized grains can also be attributed to grain boundary sliding (e.g., Bestmann and Prior, 2003; Halfpenny et al., 2006). However, if quartz is fully recrystallized during post- and inter-seismic periods, the evidence involving parent grains is largely or completely lost.

Microcracks generated, in quartz for example, at FVT depths are expected to heal rapidly (e.g., Smith and Evans, 1982; Hickman and Evans, 1987), but are typically decorated with fluid inclusions (FIs) (e.g., Roedder, 1984; Anders et al., 2014). If these FI planes (FIPs) were preserved, microcrack densities could be measured as is done in near-surface faults (e.g., Mitchell and Faulkner, 2009), providing a measure of damage-zone width. However, quartz at these depths undergoes plastic deformation by processes such as dislocation creep and grain boundary migration. During recrystallization, trapped FIs can be dragged by migrating subgrain and grain boundaries, thus disrupting their planar structure, displaying FI distribution around grain boundaries, and clearing FIs from grain interiors (Kerrich, 1976; Wilkins and Barkas, 1978; Drury and Urai, 1990; Schenk and Urai, 2005; Schmatz and Urai, 2010, 2011). Hence, counting FIPs (healed microfractures) per unit length to estimate damage-zone width (e.g., Mitchell and Faulkner, 2009) is no longer possible. However, unless the FIs are destroyed during recrystallization, the measured abundance of FIs may be related to the initial abundance of transient microfractures.

In this paper, to evaluate whether FI abundance can provide evidence for brittle co-seismic deformation at depth, we investigated FIs in monomineralic quartz aggregates across a deeply exhumed seismogenic strike-slip fault/shear zone from FVT depths (Sandhill Corner shear zone of the Norumbega fault system, Maine, USA; Johnson et al., 2009; Price et al., 2012, 2016). Since fluid-filled pores along grain boundaries may also be introduced by creep cavitation during grain boundary sliding (e.g., Blanchard and Chan, 1993; Mancktelow et al., 1998; Kassner and Hayes, 2003; Fusseis et al., 2009; Menegon et al., 2015) or Zener-Stroh cracking during dislocation creep (e.g., Stroh, 1957; Gilgannon et al., 2017), it is important to first determine the quartz deformation mechanisms in the study area. We analyzed microfabrics of quartz by electron backscatter diffraction (EBSD) to examine its deformation mechanisms during seismic cycles. In order to determine the width of co-seismic damage adjacent to the Sandhill Corner shear zone at the FVT, we present the number density (count per unit area) of FIs measured in quartz by optical observation, and provide a conceptual model of FI abundance evolution across the shear zone during a seismic cycle. Another method of measuring FI abundance through scanning electron microscope secondary electron (SEM-SE) imaging was used to compare with the optical analysis. For clarity, this paper considers only distribution and abundance of FIs; their compositions and homogenization temperature will be analyzed in a separate study to constrain the physical and chemical environment at the time of FI entrapment (e.g., Fall and Bodnar, 2018).

2. The Sandhill Corner shear zone

2.1. Geologic setting

The Sandhill Corner shear zone (SCSZ) is the longest continuous strand in the Norumbega fault system (Fig. 2; Johnson et al., 2009; Price et al., 2012, 2016). The Norumbega fault system is a long-lived, Paleozoic, large-displacement, right-lateral strike-slip fault system in the northeastern Appalachians, USA (Ludman and West, 1999), and seismic reflection data suggest that it offsets the Moho (Doll et al., 1996). Currently exposed rocks in the Norumbega fault system are upper amphibolite facies in the southwest to sub-greenschist facies in the northeast because of different erosion levels (Ludman and West, 1999). Thus, the Norumbega fault system is an ancient analogue to active, large-displacement strike-slip fault systems at mid-crustal depths such as the San Andreas fault. The SCSZ (~230 m wide in the study area) located in the central part of the Norumbega fault system contains mutually overprinting pseudotachylyte and mylonite (Price et al., 2012), indicating coeval frictional and viscous deformation during seismogenic cycles and thus a seismically active zone at FVT depths (Handy et al., 2007). The shear zone in the study area has its core at the contact between the quartzo-feldspathic Cape Elizabeth Formation and the schistose Crummett Mountain Formation (Fig. 2; Grover and Fernandes, 2003; West and Peterman, 2004; Price et al., 2016). The Cape Elizabeth Formation as a parent rock of the quartzo-feldspathic (QF) unit on the northwest side of the SCSZ is a quartz-plagioclase-biotite±garnet±sillimanite metasedimentary rock that underwent partial migmatization and upper amphibolite-facies metamorphism (Grover and Fernandes, 2003; West and Peterman, 2004). The Crummett Mountain Formation (West and Peterman, 2004; equivalent to Scarboro Formation of Grover and Fernandes, 2003) as a parent rock of the schist unit on the southeast side of the SCSZ is a quartz-plagioclase-garnet-staurolite-andalusite mica schist with discontinuous, complexly-folded quartz veins. The SCSZ is characterized by a ~200 m-wide protomylonite to mylonite in the QF unit, a ~5 m-wide ultramlonite/phyllonite in the shear zone core, and a ~25 m-wide highly-sheared schist in the schist unit (Fig. 3a; Price et al., 2016). The collected samples have subvertical foliations sub-parallel to the strike of the SCSZ, and subhorizontal stretching lineations (Price et al., 2016). The degree of mylonitization generally increases toward the shear zone core based on qualitative observations of more mica-rich matrix and higher aspect ratio of quartz domain toward the core (Fig. 3c) although mica in the matrix could be formed by pre-kinematic reactions (e.g., Menegon and Pennacchioni, 2010; Kilian et al., 2011). Price et al. (2016) estimated that mylonitic deformation, overprinting previous higher-temperature microstructures present outside the shear zone, occurred at temperatures of ~400–500 °C (corresponding to ~13–17 km in depth assuming a geothermal gradient of 30 °C/km) based on quartz (dislocation creep and subgrain rotation recrystallization) and feldspar (fracturing) deformation.

Undeformed and deformed pseudotachylytes are found in the SCSZ, especially within the immediate vicinity of the core (Figs. 3b and 4; Price et al., 2012). Pseudotachylyte is a glassy or very fine-grained rock, interpreted as quenched frictional melt, and widely accepted as evidence for earthquake slip in ancient faults (Sibson, 1975; Kirkpatrick and Rowe, 2013). The ~5 m-wide shear zone core with ultramylonite derived from pseudotachylyte (Fig. 3a) is considered as evidence for a long history of repeated co-seismic brittle and inter-seismic viscous deformation at the FVT (e.g., Sibson, 1980; Passchier, 1982; Price et al., 2012). The amount (area %) of pseudotachylyte in the SCSZ was measured in thin sections of rocks, and generally increases toward the core which locally contains >50 % (Fig. 3b; Price et al., 2012).

2.2. Quartz microstructures

The quartz domains analyzed for FI abundance are monomineralic quartz aggregates of deformed veins and ribbons from the QF rocks (Fig. 3a) embedded in a mica-rich matrix (Fig. 5). It is unclear whether the quartz domains originated from quartz-rich felsic layers or quartz veins formed prior to or during the seismogenic history (Price et al., 2016). The analyzed quartz domains from the QF unit are thinner than 2 mm except one sample (NFS2) with a 4.5 cm-thick vein (Fig. 6). Most of the quartz domains have longer lengths than the thin section size. Quartz in the host rock shows grain boundary migration recrystallization, whereas the SCSZ quartz was recrystallized dominantly by subgrain rotation with subsidiary grain boundary migration (Fig. 7; Price et al., 2016). The degrees of quartz recrystallization increase from the host rock toward the shear zone core, and the ~40 m-wide inner part of the mylonite contains fully recrystallized quartz domains (Fig. 7).

2.3. *Fluid inclusions in quartz*

There are four types of FIs based on their distribution (Fig. 8).

1) Type A distribution – The most common distribution in which FIs occur in and around all quartz grain boundaries (Figs. 5c and 8a).
2) Type B distribution – FIs in the interior of quartz grains rather than in FIPs (Fig. 8b). These FIs are rare in unrecrystallized parent grains (Fig. 8a), but occur in some recrystallized quartz domains (Figs. 8b and 8c).
3) Type C distribution – FIPs inside parent quartz grains, commonly associated with recrystallization (Fig. 8c). These FIPs lie subparallel to the mylonitic foliation, and do not extend to other phases. In the recrystallized quartz along FIPs, their planar structures are

disrupted, displaying FIs distribution along recrystallized grain boundaries and in grain interiors (Fig. 8c).

4) Type D distribution – FIPs crosscutting entire quartz domains and sometimes other phases such as the mica-rich matrix, at a high angle to the mylonitic foliation (Fig. 8d). These FIPs are sub-parallel to open or sealed cracks, do not have recrystallized grains, and are found in all the samples including the host rock (Figs. 5a and 8d).

Most FIs, irrespective of their distribution types, are less than 2 μm in diameter (Figs. 8 and 9). While the type A, B and D FI distributions are present in all samples from the host rock to the mylonite, FIPs associated with recrystallized grains (type C) are observed only in the mylonitic rocks. For the FI abundance analysis, we considered only the type A, B and C distributions since they include FIs trapped in quartz during its initial growth or during overprinting brittle and viscous deformation at the FVT. FIs with type D distribution were avoided because they are post-kinematic features likely formed at shallower depths during exhumation (e.g., Mancktelow and Pennacchioni, 2004).

3. Methods

Samples were cut perpendicular to the local foliation (along the XZ plane) and parallel to the local stretching lineation (the X-direction), which are both sub-parallel to the strike of the shear zone core. Doubly polished thin sections of ~30–35 μm thickness were prepared to observe microstructures and FIs using polarized light microscopy (mechanically polished with a 0.3 μm alumina suspension and chemically in a 0.02 μm colloidal silica suspension for several minutes). FI abundance was determined by measuring FI number density (count divided by background area). We optically measured the number of FIs by manually counting them in a single focal plane from plane-polarized light images (Fig. 9a; Movie S1). Each optical image was preprocessed by *ImageJ* (https://imagej.nih.gov/ij/) to remove uneven illumination and dirt/dust on lenses using a background image. Three to six quartz domains showing different FI abundances in each thin section were analyzed.

For comparison, the FI number density in the same analysis area as the optical method for several samples was also estimated from 2-D pores on carbon-coated polished surfaces of the thin sections using semi-automated analysis of SEM-SE images (×4000 magnification), similar to the techniques described in Schmatz and Urai (2011) (Fig. 9b). 10–144 SE images were taken for each quartz domain, and the stitched images were preprocessed using *ImageJ* to eliminate uneven brightness. After setting a threshold range to select only pores, they were processed using combinations of 'erode' and 'dilate' in *ImageJ*, and manually modified by comparing to the original SE images. From the modified bitmap images, we measured the number and size (equivalent circular diameter) of FIs. The FI size was not obtained by optical measurement because most FIs are too small (<2 μm) to clearly see their boundaries.

Since FIs are mostly located near and along grain boundaries, different grain boundary areas (or grain sizes) can affect the number of measured FIs. Sensitivity analysis (Fig. 10) showed that grain-size bias can be eliminated by measuring ~15 or more grains. Exceptions were made when measuring large parent grains where only parts of grain boundaries were covered. Another sensitivity analysis was conducted to examine the possible effect of 3-D heterogeneous FI distribution on the measured FI abundance by counting in-focus FIs from photomicrographs taken at different focal-plane depths (Fig. 11). All the analyses were carried out away from the phase boundaries between quartz domains and the mica-rich matrix.

Another polished thin section of sample NFS2 was prepared to investigate quartz deformation mechanisms through electron backscatter diffraction (EBSD) analysis because this particularly thick quartz vein shows various stages of mylonitization. The thin section was coated with a thin layer of carbon to prevent electron charging and analyzed using the Tescan Vega II Scanning Electron Microscope equipped with an EDAX-TSL EBSD system at the University of Maine, USA. Simultaneous chemical analysis was performed via EDAX Genesis Energy Dispersive Spectroscopy to identify and filter other phases that might be present in the quartz vein. Diffraction patterns were acquired using EDAX-TSL OIM Data Collection 5.31 software at an acceleration voltage of 20 kV, a beam current of ~6 nA, a 70° sample tilt, and high-vacuum conditions. EBSD data were collected with a square grid at step size of 2 μm. Raw indexing rates of quartz were >99 %. Post-processing of quartz EBSD data were conducted by EDAX-TSL OIM Analysis 5.31 software based on confidence index (CI) and neighboring orientations to produce clean EBSD maps. Non- and poor-indexed pixels (CI < 0.1) were replaced with well-indexed neighboring pixels of CI ≥ 0.1. The well-indexed pixels ranged between 80 % and 87 % of analyzed pixels. Grains in post-processing are defined by an internal misorientation ≤10° and a minimum grain size of 5 pixels. Crystallographic orientations for each pixel were represented as color-coded maps according to an inverse pole figure of quartz, in which the color of each pixel corresponds to the crystal direction perpendicular to the thin section (Y), as pole figures using equal area, upper-hemisphere projections, and as contoured pole density distributions calculated by a series expansion of generalized spherical harmonics using smoothing parameters with series rank of 10 and Gaussian half-width of 10° and then plotted linearly by multiples of uniform distribution (m.u.d.). For pole figures, the lineation (X) and the pole (Z) to the foliation are oriented east-west and north-south, respectively. Misorientation angle between randomly selected pixels (“random-pair”) as well as adjacent pixels (“neighbor-pair”) was calculated by selecting the minimum rotation angle (out of all symmetrically equivalent possibilities) required to bring two lattices into coincidence (Wheeler et al., 2001). Their distributions of quartz were plotted in histograms with bin width of 5° from 5° to 105°. The misorientation distribution of a purely random texture (“theoretical random”) is also shown as a black line in the histograms. Misorientation angle/axis pairs in crystal coordinates for quartz were plotted using *MTEX* (v. 5.3.0), an open-source MATLAB toolbox (Bachmann et al., 2010; https://mtex-toolbox.github.io/) from the post-processed EBSD data.

4. Quartz microfabrics

Sample NFS2 at a distance of ~77 m from the shear zone core has partially-recrystallized, large parent quartz grains up to ~3.5 mm in width and longer than the thin section, which are surrounded by fine-grained recrystallized quartz (Figs. 8c and 12). The parent quartz has the type C FIs, or FIPs with recrystallized grains, and FIs are rare in the unrecrystallized parent vein outside the FIPs, but are abundant where the vein has recrystallized (Fig. 8c). We analyzed a micro-shear zone in the parent quartz and a highly recrystallized region by EBSD (red boxes in Fig. 12).

In the micro-shear region, narrow zones of fine-grained recrystallized quartz cut through the large parent grain subparallel or at a low angle to the foliation (Figs. 13 and 14). EBSD analysis reveals that misorientation of the parent grain gradually increases to values of ~25° toward its edges where subgrains with similar size to the recrystallized quartz occur (Figs. 13b, 13c and 13f), and also shows an abrupt jump in misorientation angle by ~50–60° at the boundaries between the parent and recrystallized grains (Figs. 13c and 13f). At the transition to the inner part of the micro-shear zone, the crystallographic orientation of few new grains exhibits a misorientation angle of ~20–25° relative to the parent grain (Fig. 13c). The micro-shear zone consists of elongate recrystallized grains with a diameter of ~5–19 μm, and subgrains are also observed in some of the new grains (Fig. 13b). Crystallographic orientations of the new grains depict strong primary and weak secondary concentrations (Fig. 13e). While the weak secondary crystallographic preferred orientation (CPO) revealed by the few grains at the transition to the inner micro-shear zone is close to the parent grain orientation (Figs. 13b, 13d and 13e), most of the recrystallized grains displaying the strong primary CPO show a high misorientation angle to the parent grain orientation of ~65–90° (Fig. 13f), which is characterized by a high-angle maximum of [c] axes and low-angle maxima of <a> axes relative to the micro-shear zone (Fig. 13e). The orientation of the micro-shear zone (yellow line in Fig. 13e) is subparallel to the trace of a positive rhombohedral {r} plane of the parent quartz (dashed line in Fig. 13d). In the misorientation angle distribution of the new grains, both of random-pair and neighbor-pair exhibit excess low misorientations and deficient high misorientation angles, compared to the theoretical random distribution (Fig. 13g). Misorientation angle/axis pairs were plotted in a crystal reference frame (e.g., inverse pole figures) (Fig. 13h) to identify controlling slip systems (Lloyd et al., 1997). For low misorientation angles (<10°), the orientation of misorientation axes relates to the active slip systems to form subgrain walls by moving dislocations (e.g., Neumann, 2000; Wheeler et al., 2001; Halfpenny et al., 2012). The micro-shear zone shows that low angle misorientation (<10°) axes weakly cluster around <m> directions (Fig. 13h). The misorientation angle/axis plot of 50–60° has a strong maximum parallel to [c]-axis due to Dauphiné twins (e.g., Wheeler et al., 2001; Lloyd, 2004; Fig. 13h). In the photomicrographs of the micro-shear region, FIs are rare within the parent grain and the narrow recrystallization zones, but mostly decorating the boundaries of the micro-shear zones (Fig. 14).

The other analyzed region with highly recrystallized quartz shows similar microfabrics to the inner micro-shear zone. The recrystallized grains have a strong but different CPO from the parent quartz (Figs. 15a and 15c), and subgrains also occur in them (Fig. 15b). Both of random-pair and neighbor-pair misorientations reveal an excess of low misorientation angles and deficit of high misorientation angles in comparison to the theoretical random distribution (Fig. 15d). Misorientation axis distributions exhibit weak clusters around [c], <m> and <z> directions at low misorientation angles (<10°) and a Dauphiné twin relationship, or strong clustering close to [c]-axis in the 50–60° plot (Fig. 15e). The recrystallized quartz has high FI abundance compared to FI-poor parent grain (Fig. 16).

5. Fluid inclusion abundance across the SCSZ

FI abundance (number density) data were obtained by optical and SEM analyses from 15 and 11 samples, respectively, and plotted with respect to distance from the shear zone core to the QF host rock (Fig. 17; Table S1). Each data point in the graphs (Fig. 17) represents the FI abundance of each quartz domain (three to six domains per sample). For consistency in comparing samples, we considered only the maximum abundance of all the domains in each sample. The optical measurement of FI number density reveals a low-high-low trend with a progressive increase toward the outer edge of the mylonite zone, producing a maximum value in sample NFS2 at ~77 m from the shear zone core (Fig. 17b). The SEM analysis shows a similar abundance distribution with low-high-low steps from the core to the host rock, but lacks the progressive changes revealed by the optical data (Fig. 17c).

6. Discussion

6.1. Quartz deformation mechanisms

Quartz micro-shear zones with FIs in large porphyroclasts or parent grains have been documented in a number of experimental and natural rock studies by analysis of their microfabrics (Van Daalen et al., 1999; Vernooij et al., 2006a, 2006b; Trepmann et al., 2007, 2017; Menegon et al., 2008; Kjøll et al., 2015; Goncalves et al., 2016). At upper- to mid-crustal levels, micro-shear zones can be initiated by fracturing of host quartz, not necessarily related to co-seismic deformation, along intracrystalline planes such as the positive and negative rhomb, the prism, and the basal plane depending on the crystallographic orientation with respect to the stress field (Van Daalen et al., 1999; Vernooij et al., 2006b; Menegon et al., 2008; Kjøll et al., 2015; Goncalves et al., 2016). And then new grains can be formed by progressive rigid-body rotation of small fragments along the fracture (Van Daalen et al., 1999; Vernooij et al., 2006b), or by precipitation from a fluid phase into the fracture (Vernooij et al., 2006a; Menegon et al., 2008; Kjøll et al., 2015; Goncalves et al., 2016). Although the precipitation mechanism of the new grain development may explain the jump in misorientation angle between the parent and recrystallized grains (Fig. 13f), the micro-shear zones of sample NSF2 do not display evidence of precipitation as shown in Kjøll et al. (2015) and Goncalves et al. (2016), for example, secondary phases of micas, calcite and epidote (Fig. 14). Rather, our EBSD microfabrics in the micro-shear region (Figs. 13 and 14) exhibit evidence of: (a) crystal-plastic deformation such as dislocation creep with a dominant slip system of (c)<a> for tilt boundaries (interpreted from clustering of the low angle misorientation axes around {m} directions; e.g., Neumann, 2000; Lloyd, 2004), including a strong CPO and misorientation angle distributions with excess low and deficient high misorientations; (b) subgrain rotation recrystallization with low misorientation angles (~20–25°) between the parent and adjacent new grains as well as subgrains of the parent with similar size to the adjacent new grains; and (c) brittle deformation involving FI trails along the boundaries of the micro-shear zones, which may explain high misorientation angles (~50–60°) between the parent and recrystallized grains.

These observations are in agreement with the experimental results simulating deformation during the seismic cycle at depth by Trepmann et al. (2007) and the natural shear-zone rock of Trepmann et al. (2017), indicating high-stress deformation with microcracking followed by nucleation and grain growth at slowly relaxing stresses and then continuous deformation of new grains by a combination of subgrain rotation and grain boundary migration recrystallization. Furthermore, the microfabrics of the highly recrystallized region indicate dislocation creep as a dominant deformation mechanism in the post- and inter-seismic periods, based on the strong CPO, misorientation distributions with excess low and deficient high misorientation angles, and misorientation axis distribution of subgrain boundaries (clustering around [c], <m> and <z> directions, interpreted as {m}<a>, (c)<a> and {π}<a> slip systems, respectively; e.g., Neumann, 2000; Lloyd, 2004) (Fig. 15). The FI distributions along the boundaries of the micro-shear zones (Fig. 14) may also be explained by transient intragranular microcracking followed by nucleation of new grains and growth by strain-induced grain boundary migration, which dragged the FIs toward recrystallized grain boundaries (Schenk and Urai, 2005; Schmatz and Urai, 2010) and finally concentrated the FIs along the edges of the recrystallization zone owing to continued recrystallization. The FIs of the highly recrystallized region (Fig. 16) are also thought as results of repeating the processes explained above.

6.2. Origin of the fluid inclusions in the mylonite with high abundance

FIs are formed during crystal growth (primary inclusions) or associated with deformation (secondary inclusions) (e.g., Roedder, 1984). Even though the amount of primary FIs could vary in each quartz domain, and their contribution to the measured FI abundance is unknown, the systematic variation (low-high-low trend) in FI abundance with respect to distance from the shear zone core (Fig. 17b) appears to indicate that most of the FIs in the high abundance region (mylonite) are secondary inclusions. We discuss possible origins of secondary FIs in the mylonite related to deformation styles before delving into the causes of the systematic variation in FI abundance.

6.2.1. Brittle versus viscous deformation

FIs can be introduced by microcracking (e.g., Roedder, 1984; Anders et al., 2014) and distributed along grain boundaries by recrystallization (Kerrich, 1976; Wilkins and Barkas, 1978; Drury and Urai, 1990; Schenk and Urai, 2005; Schmatz and Urai, 2010, 2011). On the other hand, FIs or pores along grain boundaries can be formed during grain boundary sliding by creep cavitation (e.g., Blanchard and Chan, 1993; Mancktelow et al., 1998; Kassner and Hayes, 2003; Fusseis et al., 2009; Menegon et al., 2015). Creep cavitation along grain boundaries, especially at high angles to a dominant slip direction, can also occur during dislocation creep by Zener-Stroh cracking due to dislocation pile-up (e.g., Stroh, 1957; Gilgannon et al., 2017). If viscous deformation by grain boundary sliding and/or dislocation creep is the main cause for FI generation in the SCSZ mylonite, then the number or size of FIs would increase with more strain until quartz domains are disaggregated (e.g., Gilgannon et al., 2017) or cavities are filled with new precipitating phases (e.g., Précigout et al., 2017). However, most FIs are of similar size (<2 μm) throughout the SCSZ (Figs. 8, 9 and 10), and it appears that highly deformed quartz domains have varying amounts of FIs; for example, more FIs in the highly recrystallized quartz of sample NSF2 (Fig. 16) and less FIs in the fully recrystallized inner mylonite of sample 75 (Fig. 17a) than the less deformed micro-shear region of sample NSF2 (Fig. 15). In addition, creep cavitation by viscous deformation cannot explain the formation of FIs within grains (type B; Figs. 8b) and FIPs (type C; Figs. 8c). Therefore, although creep cavitation by grain boundary sliding and Zener-Stroh cracking during dislocation creep cannot be completely ruled out as a FI or pore formation mechanism in the SCSZ, we interpret the FIs in the mylonite to have been introduced primarily through brittle deformation by microcracking.

6.2.2. Timing of brittle deformation

Fracturing in quartz porphyroclasts along several crystallographic planes is common during the initiation of micro-shear zones in the middle crust (e.g., Van Daalen et al., 1999; Menegon et al., 2008; Kjøll et al., 2015). This type of initiation may introduce FIs to the micro-shear zone of sample NSF2 subparallel to the trace of a {r} plane of the parent quartz (dashed line in Fig. 13d) because the maximum elastic compliance in α-quartz is nearly parallel to <r> directions (McSkimin et al., 1965; Lloyd, 2000; Menegon et al., 2011). Such fracturing in sample NSF2 is more likely related to co-seismic deformation of the SCSZ since FIPs with recrystallized grains (type C FI distribution) are found only within ~80 m of the shear zone core, and the protomylonite samples do not have micro-shear zones with FI trails but show subgrain rotation recrystallization microstructures (e.g., Figs. 5b and 8a) with low FI abundance (Fig. 17).

Alternating brittle and viscous deformation in quartz occurs at the FVT during seismic cycles (Fig. 1; e.g., Handy et al., 2007; Hirth and Beeler, 2015). Therefore, we interpret the FIs observed in the SCSZ within ~80 m of the core as having their origins in the seismic cycle, most likely from co-seismic damage during rupture propagation, but potentially also from very high strain-rate flow occurring immediately after major co-seismic events. Evidence supporting this interpretation includes the following.

1) The shear zone within ~80 m of the core has considerably higher FI abundance (up to ~10 times) than the host rock (Fig. 17b).
2) FIs were introduced by brittle deformation as seen in sample NFS2 at ~77 m from the core (Fig. 8c). In the parent quartz of the sample, FIs line healed fractures. Portions of these healed fractures have recrystallized, and in these locations, the FIs are concentrated along the new grain boundaries, as is observed in recrystallized domains of the other samples (e.g., Fig. 10).
3) Recrystallization that redistributed FIs along grain boundaries occurred while the shear zone was seismically active (e.g., Price et al., 2012, 2016).
4) The inner ~40 m of the shear zone contains pseudotachylyte with locally ~8–67 % of thin-section area (Figs. 3b and 4), demonstrating that at least these rocks were directly affected by co-seismic stresses related to rupture propagation. Rupture surfaces generate a higher number of fractures in their vicinity (e.g., Mitchell and Faulkner, 2009) due to dynamic stress changes near the propagating rupture fronts (Andrews, 2005; Rice et al., 2005). Dynamic fragmentation in the inner part of the QF unit (~63 m wide) demonstrated by Song et al. (2020) using particle size distributions of fragmented garnet grains supports the role of rupture propagation in the brittle deformation that introduced FIs.

6.3. Reliable measure of FI abundance

The discrepancy in the number density data between the optical and SEM measurements (Figs. 17b and 17c) can be attributed to polishing defects and/or heterogeneous 3-D distribution of FI. While the optical method uses only FIs within the thin section away from its top and bottom surfaces, the SEM analysis requires FIs on the polished surface to be preserved as pits. Polishing processes can create new pits and/or eliminate preexisting pits by decreasing their topography on this surface. In addition, the concentration of FIs along grain boundaries may cause a heterogeneous distribution in 3-D within sections, which affects both the SEM and optical results. The sensitivity analysis for the possible effect of 3-D heterogeneous FI distribution on the abundance data in Fig. 11 shows relatively small variations compared to the overall abundance distribution (Fig. 17b). Comparing the results from the two methods, the SEM method reports lower number densities for most samples (Table S1). Thus, the discrepancy between the optical and SEM results comes mostly from polishing defects, mainly elimination of surface pits. Schmatz and Urai (2011) demonstrated that hand-polishing can provide information on real 2-D porosity within standard errors in comparison with measurements on broad ion beam-polished surfaces. However, when measuring the number of fine isolated pores (<2 μm diameter), polishing defects appear to remove topography around pores. Therefore, the more laborious optical method appears to be more accurate than the semi-automated SEM analysis for calculating FI number density, at least in instances where the pore size is small.

6.4. Possible mechanisms for lower FI abundance in the inner mylonite

Given that the shear zone core has the largest amount of pseudotachylyte in the SCSZ (Fig. 3b; Price et al., 2012), co-seismic energy would likely have generated the highest FI abundance there, with continuous decrease away from the core. We would expect this pattern to be similar to fracture density patterns in the upper crust showing a logarithmic, exponential, or power decay with distance from the fault core (e.g., Chester et al., 2005; Mitchell and Faulkner, 2009; Savage and Brodsky, 2011). Given this expectation, the observed low number density in the inner mylonite compared to the outer mylonite (Fig. 17b) may be explained by removal of FIs through viscous creep (clearing FIs from grain interiors via recrystallization) during post- and inter-seismic periods (Kerrich, 1976; Wilkins and Barkas, 1978; Drury and Urai, 1990; Schenk and Urai, 2005; Schmatz and Urai, 2010, 2011). Another potential mechanism for removing FIs is for migrating grain boundaries to drag inclusions to the mica-rich phase boundaries adjacent to the quartz aggregates. We speculate that once the grain boundaries carrying FIs reach the phase boundaries, the FIs would be lost from the recrystallizing quartz aggregate. This process may partially explain the variations in number density for different quartz domains in a sample (Fig. 17b). This mechanism is supported by the experimental study of Palazzin et al. (2018), which found that recrystallization of FI-rich quartz porphyroclasts lead to a decrease in FI abundance and H_2O content, and the latter is similar to the value of surrounding finer quartz matrix.

If quartz domain thickness is considered a proxy for its strain and age (acknowledging that quartz domains may initially have formed with varying thicknesses), there is a positive correlation between number density and domain thickness (Fig. 18). Therefore, both mechanisms would suggest a negative correlation between number density and strain; in other words, the rocks with higher degree of recrystallization would remove FIs more efficiently during the long-term inter-seismic period, contributing to the progressive decrease in number density toward the core from the outer mylonite (Figs. 7 and 17b).

6.5. Estimating width of off-fault damage in the SCSZ

In summary, we suggest that post- and inter-seismic recrystallization decreased the number of FIs more effectively in the extensively recrystallized inner mylonite than in the outer part of the mylonite, and hence the trend of low-high-low FI number density with distance from the shear zone core may be characteristic of strike-slip faults near the base of the seismogenic zone where viscous creep processes are active. This produces a paradoxical situation that more co-seismic damage in quartz at the FVT is revealed by low FI regions (with fully recrystallized quartz) instead of high FI regions (with partial recrystallization), which appears to contradict the conventional view of higher fracture (or FIP) density in quartz indicative of more damage in the brittle upper crust. However, the FI removal mechanism through post- and inter-seismic recrystallization appears to best describe the low-high-low trend in the SCSZ, regardless of whether or not some FIs were introduced by creep cavitation during viscous deformation (section 6.2.1).

In weighing all the evidence, we suggest that the region from the inner mylonite to the peak FI abundance rock (~80 m wide) may indicate a minimum width of off-fault damage in the SCSZ, corresponding to a change of 'slope' from positive to negative in the graph of Fig. 17b (see the conceptual model in Fig. 19 and the following sections). We note that this is similar to the width of dynamic fragmentation of ~63 m determined in the QF rocks by Song et al. (2020) using particle size distributions of fragmented garnet grains. In an attempt to further explore the processes affecting FI abundance in the inner mylonite, we propose a conceptual model of time-dependent FI abundance in quartz at the FVT during a seismic cycle (Fig. 19).

6.5.1. Conceptual model of FI abundance evolution during a seismic cycle

The purpose of modeling time-dependent FI abundance is to visualize the processes causing FI production and removal discussed in this study using simple equations. We made several assumptions to simplify the model and to fit the data in Fig. 17b: (a) before an earthquake, FI abundance exhibits a homogeneous background distribution across the shear zone; (b) FIs are introduced to the shear zone only by co-seismic rupture propagation in/near the core, with a linearly decreasing trend from the core to the shear zone boundary; (c) FIs are removed from quartz domains by accumulated strain and recrystallization after the co-seismic event; (d) post-seismic strain rate is the highest in the core and decreases exponentially toward the shear zone boundary; (e) with time, the post-seismic strain rate decreases to the inter-seismic strain rate; and (f) the amount of removed FIs is proportional to the accumulated strain, or the degree of recrystallization. The equations that govern the model are arbitrary and conform to the above assumptions. We note that there are cases where relatively low-strain fault rocks may show a high degree of recrystallization by, for example, pulverization followed by static grain growth (e.g., Austrheim et al., 2017; Petley-Ragan et al., 2019). However, the SCSZ recrystallized quartz does not show strong evidence of static recrystallization such as straight grain boundaries and equant grain shape, but rather exhibits shape-preferred orientation and subgrains (Figs. 7, 10 and 16). Thus, in this model, it is assumed that the fully recrystallized mylonitic rocks experienced more strain than those that are not fully recrystallized.

6.5.1.1. Before earthquake (t_0)

A constant FI abundance across the shear zone was assumed as background abundance prior to earthquakes (Fig. 20a). Before quartz domains experience seismic cycles, their initial FI abundance could be different. However, the amount of initial FIs would be considerably lower compared to co-seismically generated FIs. For example, the host rock has very low number density of FI relative to the mylonite (up to ~10 times lower; Fig. 17b). Here, a low number density (0.002 μm^{-2}) close to the value of the host rock was taken as the background FI abundance.

6.5.1.2. Co-seismic period (t_1)

For simplicity, it is assumed that co-seismic energy reaches the shear zone boundary, and the amount of FIs added by brittle co-seismic deformation shows a linear decrease with distance from the core (Fig. 20b):

$$\text{number density } [\#/\mu\text{m}^2] = -a \times \text{distance } [\text{m}] + b \quad (1)$$

where a is gradient and b is critical FI number density [#/μm^2]. Here 0.000225 for a and 0.045 for b are used to fit to the data shown in Fig. 17b after all the equations are applied, but both values would be dependent on fault conditions. The t_1 graph in Fig. 20b is drawn by adding Eq. (1) to the background FI abundance. Although a logarithmic, exponential, or power decay in fracture density from the fault core to the host rock is observed in the upper crust (e.g., Chester et al., 2005; Mitchell and Faulkner, 2009; Savage and Brodsky, 2011), no published study, to our knowledge, has investigated the relationship between the number of healed microfractures and the number of FIs. Such decay trends would have higher fracture density near the core relative to the middle of the shear zone compared with a linear trend, but would not impact the fundamental results of our model. Although we assume that co-seismic events represent the only addition of FI to the shear zone, very high strain-rate flow immediately after major rupture events may contribute to additional microcracking or creep cavitation and thus FIs. However, in this case, more FIs would be introduced near the shear zone core than the outer part of the shear zone owing to higher strain rate near the core. Therefore, the total FI addition trend would not differ significantly from the co-seismic trend.

6.5.1.3. Post- and inter-seismic periods (t_2 and t_3)

We discretized the model into nine time steps (n_1 to n_9 in Fig. 20c) during post- and inter-seismic periods. We assumed that each time step represents an exponential decrease in strain rate or strain with distance from the shear zone core. From the initial post-seismic time step (n_1) to the inter-seismic time (n_9), the strain rate and the slope of its trend decrease. Consequently, the accumulated strain in each time step also exhibits an exponential decay from the core to the shear zone boundary (Fig. 20d). From n_1 to n_9, the amount of accumulated strain increases. We also assumed that these accumulated strain trends are proportional to removal of FIs from quartz domains for each time step. The FI removal equation at each time step used in our model is as follows:

$$\text{number density } [\#/\mu\text{m}^2] = (1-0.1n)\left(c \times e^{-k\times \text{distance [m]}} + d\right); \quad n \in [1,9] \qquad (2)$$

where n is the discrete (integer) time step, c is constant, k is FI removal gradient and d is background FI removal number density [#/μm^2]. Here 0.001 for c, 0.016 for k and 0.00002 for d are used to fit to the data shown in Fig. 17b after all the equations are applied, but these values would be dependent on fault/shear zone conditions. The accumulated FI removal equation in each time step is as follows:

$$\text{number density } [\#/\mu\text{m}^2] = \sum_{n=1}^{9} \text{Eq. (2)} \qquad (3)$$

where *n* is the integer time step. Post-seismic (n_3) and the inter-seismic (n_9) time steps for FI removal are plotted in Fig. 20e as examples. The surviving FIs in the post- and inter-seismic periods is calculated by subtracting the FI removal Eq. (3) from the FI production Eq. (1) plus the background FI abundance, and plotted in Fig. 20f. The inter-seismic FI number density graph (t_3 in Figs. 19 and 20f) shows a slope change from positive to negative with distance from the shear zone core, which closely mimics our optical data in Fig. 17b. Regions far from the core in the shear zone (dashed lines in Fig. 19) would have much less co-seismic microcracking than the core even if co-seismic energy might reach the regions, and thus viscous deformation would cover traces of the microcracking there. Hence, there is uncertainty in identifying the damage-zone boundary in the outer part of the shear zone without clear evidence such as the type C FI distribution (partially-recrystallized FIP) as seen in Fig. 8c. However, the slope change in both our data and model (Figs. 17b and 19) may be used to estimate a minimum width of off-fault damage, i.e. ~80 m-wide region from the shear zone core to sample NSF 2 with the highest FI number density. This appears to be a reasonable approach at the FVT since the FI abundance both near and far from the rupture surface is lower than the intermediate distance, which is different from the upper crustal faults where their damage zones are identified by higher density of healed microcracks (FIPs) than the host rock (e.g., Mitchell and Faulkner, 2009) owing to no modification of the created microcracks at shallow depths.

6.6. Implications of off-fault damage near the base of the seismogenic zone

Our data suggest that at least a ~80 m-wide damage zone occurs near the base of the seismogenic zone in an exhumed strike-slip fault/shear zone of width ~230 m where quartz deformed viscously at ~400–500 °C (equivalent to ~13–17 km in depth using 30 °C/km thermal gradient) during post- and inter-seismic periods. This is similar to the ~63 m width of dynamic fragmentation estimated by Song et al. (2020) using particle size distributions of fragmented garnet grains in the same study area. Such deep penetration of damage in mature strike-slip faults, recently confirmed by Ben-Zion and Zaliapin (2019), would facilitate transient fluid flow and rheological changes by modifying permeability (e.g., Mitchell and Faulkner, 2008) and thermal structure (e.g., Morton et al., 2012) within and surrounding the fault/shear zone core. The ~80 m-wide damage zone in the SCSZ is also consistent with recent numerical results (Okubo et al., 2019), which predicted a damage zone width of ~100 m at 10 km depth. In the SCSZ, the estimated minimum width of off-fault damage roughly corresponds to the outer edge of the mylonite (~90 m from the core) (Fig. 19). This correlation between co-seismic damage and mylonitization suggests that the inner mylonite, containing fully recrystallized quartz domains and extending ~40 m from the shear zone core, experienced intensive co-seismic fracturing and possibly pulverization (Song et al., 2020). This implies that off-fault damage at depth facilitates grain size reduction of quartz by both brittle fragmentation and dynamic recrystallization and thus acts as a significant factor contributing to strain localization near the base of the seismogenic zone. Prando et al. (2020) also found a similar correlation between the thickness of the damage zone (~1 m from the fault core) and the thickness of the mylonite (0.6–1 m wide) in a smaller strike-slip fault zone at the FVT (400–500 °C and 3–4 kbar). The fault zone of Prando et al. (2020) is much smaller than the SCSZ, and thus this might indicate that the width of the ductile shear zone exerts a first order control on the geometry and distribution of a brittle damage zone at the FVT.

7. Conclusions

1. The pseudotachylyte-bearing SCSZ exhumed from the FVT at ~400–500 °C records alternating co-seismic brittle and post-/inter-seismic viscous deformation in quartz, evidenced by FIPs overprinted by recrystallized grains. This is also supported by microfabrics of micro-shear zones cutting through large parent quartz grains, such as an abrupt jump in crystal misorientation and marked CPO of recrystallized quartz within the micro-shear zone.
2. FIs in the SCSZ quartz are distributed mostly along and near grain boundaries and infrequently in grain interiors. The optically measured FI number density in quartz domains reveals a systematic trend of low-high-low with a progressive increase from the shear zone core toward the outer mylonite, which is different from upper crustal faults that show a continuous high-low trend of microfracture density away from the fault core. Removal of FIs from grain interiors and ultimately quartz domains, via recrystallization, can explain the low FI abundance in the highly recrystallized inner mylonite of the SCSZ.
3. The low-high-low trend of FI abundance may be characteristic of strike-slip fault/shear zones near the base of the seismogenic zone (in the FVT) since post- and inter-seismic recrystallization decreases the number of FIs more effectively in the extensively recrystallized inner mylonite. The minimum width of off-fault damage may be indicated by the ~80 m-wide region from the fully recrystallized inner mylonite with low FI abundance to the outer mylonite with the peak FI abundance, corresponding to a change of 'slope' from positive to negative in the FI abundance graph with respect to distance from the shear zone core.
4. Co-seismic damage zones in large-displacement strike-slip faults can extend to the base of the seismogenic zone, implying significant contribution to viscous strain localization

in the FVT, demonstrated by grain size reduction of quartz through both brittle fracturing and dynamic recrystallization.

Acknowledgements

We thank András Fall and Luca Menegon for their thorough and constructive reviews. This research was supported by National Science Foundation grants EAR-1727090 and EAR-0820946.

References

Anders, M.H., Laubach, S.E., Scholz, C.H., 2014. Microfractures: A review. Journal of Structural Geology 69, 377–394. https://doi.org/10.1016/j.jsg.2014.05.011.

Andrews, D.J., 2005. Rupture dynamics with energy loss outside the slip zone. Journal of Geophysical Research 110, B01307. https://doi.org/10.1029/2004JB003191.

Austrheim, H., Dunkel, K.G., Plümper, O., Ildefonse, B., Liu, Y., Jamtveit, B., 2017. Fragmentation of wall rock garnets during deep crustal earthquakes. Science Advances 3, e1602067. https://doi.org/10.1126/sciadv.1602067.

Bachmann, F., Hielscher, R., Schaeben, H., 2010. Texture analysis with MTEX- Free and open source software toolbox. Solid State Phenomena 160, 63–68. https://doi.org/10.4028/www.scientific.net/SSP.160.63.

Ben-Zion, Y., 1998. Properties of seismic fault zone waves and their utility for imaging low-velocity structures. Journal of Geophysical Research 103, 12567–12585. https://doi.org/10.1029/98jb00768.

Ben-Zion, Y., Peng, Z., Okaya, D., Seeber, L., Armbruster, J.G., Ozer, N., Michael, A.J., Baris, S., Aktar, M., 2003. A shallow fault-zone structure illuminated by trapped waves in the Karadere–Duzce branch of the North Anatolian Fault, western Turkey. Geophysical Journal International 152, 699–717. https://doi.org/10.1046/j.1365-246X.2003.01870.x.

Ben-Zion, Y., Sammis, C.G., 2013. Shear heating during distributed fracturing and pulverization of rocks. Geology 41, 139–142. https://doi.org/10.1130/G33665.1.

Ben-Zion, Y., Sammis, C.G., 2003. Characterization of fault zones. Pure and Applied Geophysics 160, 677–715. https://doi.org/10.1007/pl00012554.

Ben-Zion, Y., Zaliapin, I., 2019. Spatial variations of rock damage production by earthquakes in southern California. Earth and Planetary Science Letters 512, 184–193. https://doi.org/10.1016/j.epsl.2019.02.006.

Bestmann, M., Prior, D.J., 2003. Intragranular dynamic recrystallization in naturally deformed calcite marble: diffusion accommodated grain boundary sliding as a result of subgrain rotation recrystallization. Journal of Structural Geology 25, 1597–1613. https://doi.org/10.1016/S0191-8141(03)00006-3.

Blanchard, C.R., Chan, K.S., 1993. Evidence of grain-boundary-sliding-induced cavitation in ceramics under compression. Journal of the American Ceramic Society 76, 1651–1660. https://doi.org/10.1111/j.1151-2916.1993.tb06631.x.

Cappa, F., Perrin, C., Manighetti, I., Delor, E., 2014. Off-fault long-term damage: A condition to account for generic, triangular earthquake slip profiles. Geochemistry, Geophysics, Geosystems 15, 1476–1493. https://doi.org/10.1002/2013GC005182.

Castro, R.R., Ben-Zion, Y., 2013. Potential signatures of damage-related radiation from aftershocks of the 4 april 2010 (M_w7.2) El Mayor-Cucapah earthquake, Baja California, México. Bulletin of the Seismological Society of America 103, 1130–1140.

https://doi.org/10.1785/0120120163.

Chester, F.M., Evans, J.P., Biegel, R.L., 1993. Internal structure and weakening mechanisms of the San Andreas fault. Journal of Geophysical Research 98, 771–786. https://doi.org/10.1029/92JB01866.

Chester, J.S., Chester, F.M., Kronenberg, A.K., 2005. Fracture surface energy of the Punchbowl fault, San Andreas system. Nature 437, 133–136. https://doi.org/10.1038/nature03942.

Cochran, E.S., Li, Y.-G., Shearer, P.M., Barbot, S., Fialko, Y., Vidale, J.E., 2009. Seismic and geodetic evidence for extensive, long-lived fault damage zones. Geology 37, 315–318. https://doi.org/10.1130/G25306A.1.

Doll, W.E., Domoracki, W.J., Costain, J.K., Çoruh, C., Ludman, A., Hopeck, J.T., 1996. Seismic reflection evidence for the evolution of a transcurrent fault system: The Norumbega fault zone, Maine. Geology 24, 251–254. https://doi.org/10.1130/0091-7613(1996)024<0251:SREFTE>2.3.CO;2.

Dor, O., Ben-Zion, Y., Rockwell, T.K., Brune, J., 2006. Pulverized rocks in the Mojave section of the San Andreas Fault Zone. Earth and Planetary Science Letters 245, 642–654. https://doi.org/10.1016/j.epsl.2006.03.034.

Drury, M.R., Urai, J.L., 1990. Deformation-related recrystallization processes. Tectonophysics 172, 235–253. https://doi.org/10.1016/0040-1951(90)90033-5.

Fall, A., Bodnar, R.J., 2018. How precisely can the temperature of a fluid event be constrained using fluid inclusions? Economic Geology 113, 1817–1843. https://doi.org/10.5382/econgeo.2018.4614.

Faulkner, D.R., Jackson, C.A.L., Lunn, R.J., Schlische, R.W., Shipton, Z.K., Wibberley, C.A.J., Withjack, M.O., 2010. A review of recent developments concerning the structure, mechanics and fluid flow properties of fault zones. Journal of Structural Geology 32, 1557–1575. https://doi.org/10.1016/j.jsg.2010.06.009.

Faulkner, D.R., Mitchell, T.M., Healy, D., Heap, M.J., 2006. Slip on 'weak' faults by the rotation of regional stress in the fracture damage zone. Nature 444, 922–925. https://doi.org/10.1038/nature05353.

Faulkner, D.R., Mitchell, T.M., Jensen, E., Cembrano, J., 2011. Scaling of fault damage zones with displacement and the implications for fault growth processes. Journal of Geophysical Research 116, B05403. https://doi.org/10.1029/2010JB007788.

Fusseis, F., Regenauer-Lieb, K., Liu, J., Hough, R.M., De Carlo, F., 2009. Creep cavitation can establish a dynamic granular fluid pump in ductile shear zones. Nature 459, 974–977. https://doi.org/10.1038/nature08051.

Gilgannon, J., Fusseis, F., Menegon, L., Regenauer-Lieb, K., Buckman, J., 2017. Hierarchical creep cavity formation in an ultramylonite and implications for phase mixing. Solid Earth 8, 1193–1209. https://doi.org/10.5194/se-8-1193-2017.

Goncalves, P., Poilvet, J.C., Oliot, E., Trap, P., Marquer, D., 2016. How does shear zone nucleate? An example from the Suretta nappe (Swiss Eastern Alps). Journal of Structural Geology 86, 166–180. https://doi.org/10.1016/j.jsg.2016.02.015.

Grover, T.W., Fernandes, L.C., 2003. Bedrock geology of the Weeks Mills Quadrangle, Maine. Maine Geological Survey, Open-File Map 03-49, color map, scale 1:24000. https://digitalmaine.com/mgs_maps/31/.

Halfpenny, A., Prior, D.J., Wheeler, J., 2012. Electron backscatter diffraction analysis to determine the mechanisms that operated during dynamic recrystallisation of quartz-rich rocks. Journal of Structural Geology 36, 2–15. https://doi.org/10.1016/j.jsg.2012.01.001.

Halfpenny, A., Prior, D.J., Wheeler, J., 2006. Analysis of dynamic recrystallization and nucleation in a quartzite mylonite. Tectonophysics 427, 3–14. https://doi.org/10.1016/j.tecto.2006.05.016.

Handy, M.R., Hirth, G., Bürgmann, R., 2007. Continental fault ftructure and rheology from the frictional-to-viscous transition downward. In: Handy, M.R., Hirth, G., Hovius, N. (Eds.), Tectonic Faults: Agents of Change on a Dynamic Earth. The MIT Press, 139–182. https://doi.org/10.7551/mitpress/6703.003.0008.

Hickman, S.H., Evans, B., 1987. Influence of geometry upon crack healing rate in calcite. Physics and Chemistry of Minerals 15, 91–102. https://doi.org/10.1007/BF00307614.

Hirth, G., Beeler, N.M., 2015. The role of fluid pressure on frictional behavior at the base of the seismogenic zone. Geology 43, 223–226. https://doi.org/10.1130/G36361.1.

Huang, Y., Ampuero, J., 2011. Pulse-like ruptures induced by low-velocity fault zones. Journal of Geophysical Research 116, B12307. https://doi.org/10.1029/2011JB008684.

Huang, Y., Ampuero, J., Helmberger, D. V., 2016. The potential for supershear earthquakes in damaged fault zones – theory and observations. Earth and Planetary Science Letters 433, 109–115. https://doi.org/10.1016/j.epsl.2015.10.046.

Huang, Y., Ampuero, J., Helmberger, D. V., 2014. Earthquake ruptures modulated by waves in damaged fault zones. Journal of Geophysical Research 119, 3133–3154. https://doi.org/10.1002/2013JB010724.

Jamtveit, B., Petley-Ragan, A., Incel, S., Dunkel, K.G., Aupart, C., Austrheim, H., Corfu, F., Menegon, L., Renard, F., 2019. The Effects of earthquakes and fluids on the metamorphism of the lower continental crust. Journal of Geophysical Research 124, 7725–7755. https://doi.org/10.1029/2018JB016461.

Johnson, S.E., Lenferink, H.J., Price, N.A., Marsh, J.H., Koons, P.O., West Jr., D.P., Beane, R., 2009. Clast-based kinematic vorticity gauges: The effects of slip at matrix/clast interfaces. Journal of Structural Geology 31, 1322–1339. https://doi.org/10.1016/j.jsg.2009.07.008.

Kanamori, H., Rivera, L., 2006. Energy partitioning during an earthquake. In: Abercrombie, R., McGarr, A., Di Toro, G., Kanamori, H. (Eds.), Earthquakes: Radiated Energy and the Physics of Faulting. American Geophysical Union Geophysical Monograph 170, 3–13. https://doi.org/10.1029/170GM03.

Kassner, M.E., Hayes, T.A., 2003. Creep cavitation in metals. International Journal of Plasticity 19, 1715–1748. https://doi.org/10.1016/S0749-6419(02)00111-0.

Kerrich, R., 1976. Some effects of tectonic recrystallisation on fluid inclusions in vein quartz. Contributions to Mineralogy and Petrology 59, 195–202. https://doi.org/10.1007/BF00371308.

Kilian, R., Heilbronner, R., Stünitz, H., 2011. Quartz grain size reduction in a granitoid rock and the transition from dislocation to diffusion creep. Journal of Structural Geology 33, 1265–1284. https://doi.org/10.1016/j.jsg.2011.05.004.

Kirkpatrick, J.D., Rowe, C.D., 2013. Disappearing ink: How pseudotachylytes are lost from the rock record. Journal of Structural Geology 52, 183–198. https://doi.org/10.1016/j.jsg.2013.03.003.

Kjøll, H.J., Viola, G., Menegon, L., Sørensen, B.E., 2015. Brittle-viscous deformation of vein quartz under fluid-rich lower greenschist facies conditions. Solid Earth 6, 681–699. https://doi.org/10.5194/se-6-681-2015.

Li, Y.-G., Chen, P., Cochran, E.S., Vidale, J.E., Burdette, T., 2006. Seismic evidence for rock damage and healing on the San Andreas fault associated with the 2004 M 6.0 Parkfield earthquake. Bulletin of the Seismological Society of America 96, S349–S363. https://doi.org/10.1785/0120050803.

Li, Y.-G., Leary, P., Aki, K., Malin, P., 1990. Seismic trapped modes in the Oroville and San Andreas fault zones. Science 249, 763–766. https://doi.org/10.1126/science.249.4970.763.

Li, Y.-G., Malin, P.E., 2008. San Andreas Fault damage at SAFOD viewed with fault-guided waves. Geophysical Research Letters 35, L08304. https://doi.org/10.1029/2007GL032924.

Lloyd, G.E., 2004. Microstructural evolution in a mylonitic quartz simple shear zone: the significant roles of dauphine twinning and misorientation. Geological Society, London, Special Publications 224, 39–61. https://doi.org/10.1144/GSL.SP.2004.224.01.04.

Lloyd, G.E., 2000. Grain boundary contact effects during faulting of quartzite: an SEM/EBSD analysis. Journal of Structural Geology 22, 1675–1693. https://doi.org/10.1016/S0191-8141(00)00069-9.

Lloyd, G.E., Farmer, A.B., Mainprice, D., 1997. Misorientation analysis and the formation and orientation of subgrain and grain boundaries. Tectonophysics 279, 55–78. https://doi.org/10.1016/S0040-1951(97)00115-7.

Ludman, A., West Jr., D.P., 1999. Norumbega Fault System of the Northern Appalachians. Geological Society of America Special Paper 331. https://doi.org/https://doi.org/10.1130/SPE331.

Mancktelow, N.S., Grujic, D., Johnson, E.L., 1998. An SEM study of porosity and grain boundary microstructure in quartz mylonites, Simplon Fault Zone, Central Alps. Contributions to Mineralogy and Petrology 131, 71–85. https://doi.org/10.1007/s004100050379.

Mancktelow, N.S., Pennacchioni, G., 2004. The influence of grain boundary fluids on the microstructure of quartz-feldspar mylonites. Journal of Structural Geology 26, 47–69. https://doi.org/10.1016/S0191-8141(03)00081-6.

McSkimin, H.J., Andreatch, P., Thurston, R.N., 1965. Elastic moduli of quartz versus hydrostatic pressure at 25° and − 195.8°C. Journal of Applied Physics 36, 1624–1632. https://doi.org/10.1063/1.1703099.

Menegon, L., Fusseis, F., Stünitz, H., Xiao, X., 2015. Creep cavitation bands control porosity and fluid flow in lower crustal shear zones. Geology 43, 227–230. https://doi.org/10.1130/G36307.1.

Menegon, L., Pennacchioni, G., 2010. Local shear zone pattern and bulk deformation in the Gran Paradiso metagranite (NW Italian Alps). International Journal of Earth Sciences 99, 1805–1825. https://doi.org/10.1007/s00531-009-0485-6.

Menegon, L., Piazolo, S., Pennacchioni, G., 2011. The effect of Dauphiné twinning on plastic strain in quartz. Contributions to Mineralogy and Petrology 161, 635–652. https://doi.org/10.1007/s00410-010-0554-7.

Menegon, L., Pennacchioni, G., Heilbronner, R., Pittarello, L., 2008. Evolution of quartz microstructure and *c*-axis crystallographic preferred orientation within ductilely deformed granitoids (Arolla unit, Western Alps). Journal of Structural Geology 30, 1332–1347. https://doi.org/10.1016/j.jsg.2008.07.007.

Miller, S.A., Collettini, C., Chiaraluce, L., Cocco, M., Barchi, M., Kaus, B.J.P., 2004. Aftershocks driven by a high-pressure CO_2 source at depth. Nature 427, 724–727. https://doi.org/10.1038/nature02251.

Mitchell, T.M., Ben-Zion, Y., Shimamoto, T., 2011. Pulverized fault rocks and damage asymmetry along the Arima-Takatsuki Tectonic Line, Japan. Earth and Planetary Science

Letters 308, 284–297. https://doi.org/10.1016/j.epsl.2011.04.023.

Mitchell, T.M., Faulkner, D.R., 2009. The nature and origin of off-fault damage surrounding strike-slip fault zones with a wide range of displacements: A field study from the Atacama fault system, northern Chile. Journal of Structural Geology 31, 802–816. https://doi.org/10.1016/j.jsg.2009.05.002.

Mitchell, T.M., Faulkner, D.R., 2008. Experimental measurements of permeability evolution during triaxial compression of initially intact crystalline rocks and implications for fluid flow in fault zones. Journal of Geophysical Research 113, B11412. https://doi.org/10.1029/2008JB005588.

Moecher, D.P., Steltenpohl, M.G., 2009. Direct calculation of rupture depth for an exhumed paleoseismogenic fault from mylonitic pseudotachylyte. Geology 37, 999–1002. https://doi.org/10.1130/G30166A.1.

Morton, N., Girty, G.H., Rockwell, T.K., 2012. Fault zone architecture of the San Jacinto fault zone in Horse Canyon, southern California: A model for focused post-seismic fluid flow and heat transfer in the shallow crust. Earth and Planetary Science Letters 329–330, 71–83. https://doi.org/10.1016/j.epsl.2012.02.013.

Neumann, B., 2000. Texture development of recrystallised quartz polycrystals unravelled by orientation and misorientation characteristics. Journal of Structural Geology 22, 1695–1711. https://doi.org/10.1016/S0191-8141(00)00060-2.

Okubo, K., Bhat, H.S., Rougier, E., Marty, S., Schubnel, A., Lei, Z., Knight, E.E., Klinger, Y., 2019. Dynamics, radiation and overall energy budget of earthquake rupture with coseismic off-fault damage. Journal of Geophysical Research 124, 11771–11801. https://doi.org/10.1029/2019jb017304.

Orlandini, O.F., Mahan, K.H., Williams, M.J., Regan, S.P., Mueller, K.J., 2019. Evidence for deep crustal seismic rupture in a granulite-facies, intraplate, strike-slip shear zone, northern Saskatchewan, Canada. Geological Society of America Bulletin 131, 403–425. https://doi.org/10.1130/B31922.1.

Palazzin, G., Raimbourg, H., Stünitz, H., Heilbronner, R., Neufeld, K., Précigout, J., 2018. Evolution in H_2O contents during deformation of polycrystalline quartz: An experimental study. Journal of Structural Geology 114, 95–110. https://doi.org/10.1016/j.jsg.2018.05.021.

Passchier, C.W., 1982. Pseudotachylyte and the development of ultramylonite bands in the Saint-Barthélemy Massif, French Pyrenees. Journal of Structural Geology 4, 69–79. https://doi.org/10.1016/0191-8141(82)90008-6.

Perrin, C., Manighetti, I., Ampuero, J., Cappa, F., Gaudemer, Y., 2016. Location of largest earthquake slip and fast rupture controlled by along-strike change in fault structural maturity due to fault growth. Journal of Geophysical Research 121, 3666–3685. https://doi.org/10.1002/2015JB012671.

Petley-Ragan, A., Ben-Zion, Y., Austrheim, H., Ildefonse, B., Renard, F., Jamtveit, B., 2019. Dynamic earthquake rupture in the lower crust. Science Advances 5, eaaw0913. https://doi.org/10.1126/sciadv.aaw0913.

Prando, F., Menegon, L., Anderson, M., Marchesini, B., Mattila, J., Viola, G., 2020. Fluid-mediated, brittle-ductile deformation at seismogenic depth - Part 2: Stress history and fluid pressure variations in a shear zone in a nuclear waste repository (Olkiluoto Island, Finland). Solid Earth 11, 489–511. https://doi.org/10.5194/se-11-489-2020.

Précigout, J., Prigent, C., Palasse, L., Pochon, A., 2017. Water pumping in mantle shear zones. Nature Communications 8, 15736. https://doi.org/10.1038/ncomms15736.

Price, N.A., Johnson, S.E., Gerbi, C.C., West Jr., D.P., 2012. Identifying deformed pseudotachylyte and its influence on the strength and evolution of a crustal shear zone at the base of the seismogenic zone. Tectonophysics 518–521, 63–83. https://doi.org/10.1016/j.tecto.2011.11.011.

Price, N.A., Song, W.J., Johnson, S.E., Gerbi, C.C., Beane, R.J., West Jr., D.P., 2016. Recrystallization fabrics of sheared quartz veins with a strong pre-existing crystallographic preferred orientation from a seismogenic shear zone. Tectonophysics 682, 214–236. https://doi.org/10.1016/j.tecto.2016.05.030.

Rempe, M., Mitchell, T., Renner, J., Nippress, S., Ben-Zion, Y., Rockwell, T., 2013. Damage and seismic velocity structure of pulverized rocks near the San Andreas Fault. Journal of Geophysical Research 118, 2813–2831. https://doi.org/10.1002/jgrb.50184.

Rice, J.R., Sammis, C.G., Parsons, R., 2005. Off-fault secondary failure induced by a dynamic slip pulse. Bulletin of the Seismological Society of America 95, 109–134. https://doi.org/10.1785/0120030166.

Rockwell, T., Sisk, M., Girty, G., Dor, O., Wechsler, N., Ben-Zion, Y., 2009. Chemical and physical characteristics of pulverized tejon lookout granite adjacent to the San Andreas and garlock faults: Implications for earthquake physics. Pure and Applied Geophysics 166, 1725–1746. https://doi.org/10.1007/s00024-009-0514-1.

Roedder, E., 1984. Fluid Inclusions. Reviews in Mineralogy 12, Mineralogical Society of America.

Savage, H.M., Brodsky, E.E., 2011. Collateral damage: Evolution with displacement of fracture distribution and secondary fault strands in fault damage zones. Journal of Geophysical Research 116, B03405. https://doi.org/10.1029/2010JB007665.

Schenk, O., Urai, J.L., 2005. The migration of fluid-filled grain boundaries in recrystallizing synthetic bischofite: first results of in-situ high-pressure, high-temperature deformation experiments in transmitted light. Journal of Metamorphic Geology 23, 695–709. https://doi.org/10.1111/j.1525-1314.2005.00604.x.

Schmatz, J., Urai, J.L., 2011. The interaction of migrating grain boundaries and fluid inclusions in naturally deformed quartz: A case study of a folded and partly recrystallized quartz vein from the Hunsrück Slate, Germany. Journal of Structural Geology 33, 468–480. https://doi.org/10.1016/j.jsg.2010.12.010.

Schmatz, J., Urai, J.L., 2010. The interaction of fluid inclusions and migrating grain boundaries in a rock analogue: deformation and annealing of polycrystalline camphor-ethanol mixtures. Journal of Metamorphic Geology 28, 1–18. https://doi.org/10.1111/j.1525-1314.2009.00849.x.

Scholz, C.H., 1990. The Mechanics of Earthquakes and Faulting. Cambridge University Press.

Scholz, C.H., 1988. The brittle-plastic transition and the depth of seismic faulting. Geologische Rundschau 77, 319–328. https://doi.org/10.1007/BF01848693.

Shipton, Z.K., Evans, J.P., Abercrombie, R.E., Brodsky, E.E., 2006. The missing sinks: Slip localization in faults, damage zones, and the seismic energy budget. In: Abercrombie, R., McGarr, A., Di Toro, G., Kanamori, H. (Eds.), Earthquakes: Radiated Energy and the Physics of Faulting. American Geophysical Union Geophysical Monograph 170, 217–222. https://doi.org/10.1029/170GM22.

Sibson, R.H., 1980. Transient discontinuities in ductile shear zones. Journal of Structural Geology 2, 165–171. https://doi.org/10.1016/0191-8141(80)90047-4.

Sibson, R.H., 1977. Fault rocks and fault mechanisms. Journal of the Geological Society 133, 191–213. https://doi.org/10.1144/gsjgs.133.3.0191.

Sibson, R.H., 1975. Generation of pseudotachylyte by ancient seismic faulting. Geophysical Journal of the Royal Astronomical Society 43, 775–794. https://doi.org/10.1111/j.1365-246X.1975.tb06195.x.

Smith, D.L., Evans, B., 1982. Diffusional crack healing in quartz. Journal of Geophysical Research 89, 4125–4135. https://doi.org/10.1029/jb089ib06p04125.

Soda, Y., Okudaira, T., 2018. Microstructural evidence for the deep pulverization in a lower crustal meta-anorthosite. Terra Nova 30, 399–405. https://doi.org/10.1111/ter.12355.

Song, B.R., Johnson, S.E., Song, W.J., Gerbi, C.C., Yates, M.G., 2020. Coseismic damage runs deep in continental strike-slip faults. Earth and Planetary Science Letters 539, 116226. https://doi.org/10.1016/j.epsl.2020.116226.

Spudich, P., Olsen, K.B., 2001. Fault zone amplified waves as a possible seismic hazard along the Calaveras fault in central California. Geophysical Research Letters 28, 2533–2536. https://doi.org/10.1029/2000GL011902.

Stroh, A.N., 1957. A theory of the fracture of metals. Advances in Physics 6, 418–465. https://doi.org/10.1080/00018735700101406.

Sullivan, W.A., Peterman, E.M., 2017. Pulverized granite at the brittle-ductile transition: An example from the Kellyland fault zone, eastern Maine, U.S.A. Journal of Structural Geology 101, 109–123. https://doi.org/10.1016/j.jsg.2017.07.002.

Thomas, M.Y., Bhat, H.S., Klinger, Y., 2017. Effect of brittle off-fault damage on earthquake rupture dynamics. In: Thomas, M.Y., Mitchell, T.M., Bhat, H.S. (Eds.), Fault Zone Dynamic Processes: Evolution of Fault Properties During Seismic Rupture. American Geophysical Union Geophysical Monograph 227, 225–280.

https://doi.org/10.1002/9781119156895.ch14.

Trepmann, C.A., Hsu, C., Hentschel, F., Döhler, K., Schneider, C., Wichmann, V., 2017. Recrystallization of quartz after low-temperature plasticity – The record of stress relaxation below the seismogenic zone. Journal of Structural Geology 95, 77–92. https://doi.org/10.1016/j.jsg.2016.12.004.

Trepmann, C.A., Stöckhert, B., Dorner, D., Moghadam, R.H., Küster, M., Röller, K., 2007. Simulating coseismic deformation of quartz in the middle crust and fabric evolution during postseismic stress relaxation — An experimental study. Tectonophysics 442, 83–104. https://doi.org/10.1016/j.tecto.2007.05.005.

Tse, S.T., Rice, J.R., 1986. Crustal earthquake instability in relation to the depth variation of frictional slip properties. Journal of Geophysical Research 91, 9452–9472. https://doi.org/10.1029/jb091ib09p09452.

Van Daalen, M., Heilbronner, R., Kunze, K., 1999. Orientation analysis of localized shear deformation in quartz fibres at the brittle-ductile transition. Tectonophysics 303, 83–107. https://doi.org/10.1016/S0040-1951(98)00264-9.

Vernooij, M.G.C., Den Brok, B., Kunze, K., 2006a. Development of crystallographic preferred orientations by nucleation and growth of new grains in experimentally deformed quartz single crystals. Tectonophysics 427, 35–53. https://doi.org/10.1016/j.tecto.2006.06.008.

Vernooij, M.G.C., Kunze, K., Den Brok, B., 2006b. 'Brittle' shear zones in experimentally deformed quartz single crystals. Journal of Structural Geology 28, 1292–1306. https://doi.org/10.1016/j.jsg.2006.03.018.

West Jr., D.P., Peterman, E.M., 2004. Bedrock geology of the Razorville Quadrangle, Maine. Maine Geological Survey, Open-File Map 04-29, color map, scale 1:24000.

https://digitalmaine.com/mgs_maps/40/.

Wheeler, J., Prior, D.J., Jiang, Z., Spiess, R., Trimby, P.W., 2001. The petrological significance of misorientations between grains. Contributions to Mineralogy and Petrology 141, 109–124. https://doi.org/10.1007/s004100000225.

Wilkins, R.W.T., Barkas, J.P., 1978. Fluid inclusions, deformation and recrystallization in granite tectonites. Contributions to Mineralogy and Petrology 65, 293–299. https://doi.org/10.1007/bf00375515.

Figure captions

Figure 1. Deformation processes with depth during one seismic cycle, showing time-dependent variation in depth of brittle deformation (modified from Tse and Rice (1986) and Handy et al. (2007)). The horizontal time axis is not to scale; co-seismic phase is seconds to minutes, post-seismic is days to 10 years, and inter-seismic is 10 to 1000 years. The vertical depth axis is dependent on local geothermal gradients. Nucleation (hypocenter) in the seismogenic zone is marked by asterisk, and the red line depicts the frictional-to-viscous transition (FVT) or brittle-ductile transition (BDT). The FVT is confined between a long-term brittle-viscous deformation boundary (ca. 300 °C) and a maximum rupture penetration depth (schizosphere-plastophere boundary; Scholz, 1990). Note that the maximum rupture depth drawn here is only indicative; deeper co-seismic slip has been reported (e.g., Moecher and Steltenpohl, 2009; Orlandini et al. 2018). See the online article for the color version of this figure.

Figure 2. Geologic setting and study area (red box in the rightmost map) of the Sandhill Corner shear zone (SCSZ) in the Norumbega fault system (NFS), USA. See the online article for the color version of this figure.

Figure 3. Details of the Sandhill Corner shear zone (SCSZ). (a) Detailed geologic setting of the study area in Fig. 2 and sample locations. The samples for measurement of fluid inclusion (FI) abundance (white circles) and pseudotachylyte analysis (black circles) are from the quartzo-feldspathic (QF) unit. (b) Plot of area percentage of pseudotachylyte, measured at thin-section scale, with respect to perpendicular distance from the shear zone core. Note that the pseudotachylyte occurs within ~40 m of the core, locally from ~8 to ~67 % of thin-section area. (c) SCSZ microstructures showing varied degrees of mylonitization. More mica-rich matrix (blue) and higher aspect ratio of quartz domain (green) are observed toward the shear zone core. In the photomicrographs (left column), the top left number (or letter) and the top right number within parenthesis, respectively, indicate sample name and distance from the shear zone core. PPL, plane-polarized light. See the online article for the color version of this figure.

Figure 4. Photomicrograph and backscattered electron (BSE) image of deformed pseudotachylyte (sample BB44) at 24 m away from the shear zone core. Note that the pseudotachylyte between wall rocks cuts a porphyroclast of plagioclase. PPL, plane-polarized light. See the online article for the color version of this figure.

Figure 5. Photomicrographs of quartz domains embedded in mica-rich matrix. (a) Host rock quartz domain (BB7) with one grain thickness. (b) Protomylonite sample (205). (c) Outer part of

mylonite (201). (d) Inner part of mylonite (75). The top right number within parenthesis indicates distance from the shear zone core. Note more fluid inclusions in (c), mostly along grain boundaries, than the other samples. XPL, cross-polarized light; PPL, plane-polarized light. See the online article for the color version of this figure.

Figure 6. Thickness measurement of quartz domains. (a) Plot of quartz domain thickness against distance from shear zone core. Various quartz domains with different fluid inclusion abundances were selected in each sample where available. Sample numbers are displayed, and a logarithmic scale is used for the thickness axis. (b) Example of how quartz domain thickness was measured. The thickness is calculated by dividing the area of a quartz domain by the length of a neutral line, except sample NFS2 in which the quartz vein fills the entire thin section. The top right number within parenthesis indicates distance from the shear zone core. PPL, plane-polarized light. See the online article for the color version of this figure.

Figure 7. Quartz photomicrographs showing an increase in recrystallization toward the core. The top right number within parenthesis indicates distance from the shear zone core. XPL, cross-polarized light. See the online article for the color version of this figure.

Figure 8. Four types of fluid inclusion (FI) distribution. (a) Type A distribution. FIs are distributed in and near grain boundaries. This type is the most common FI distribution. The example photomicrograph is from a protomylonite. (b) Type B distribution. FIs are distributed within grains. The example in the photomicrograph taken from an outer myonite also has the type A distribution. (c) Type C distribution as a form of fluid inclusion plane (FIP) but having

recrystallized (rxd) grains. The example is a different region of the sample in (b). Note also correlation of FI abundance with rxd grains. (d) Type D distribution as a form of FIP without rxd grains crosscutting the mylonitic foliation and sometimes other phases. This is found in all the samples. XPL, cross-polarized light; PPL, plane-polarized light. See the online article for the color version of this figure.

Figure 9. Two methods to measure fluid inclusion (FI) number density (count per unit area). (a) Optical image sequence of a single FI with different focal depths. This image sequence was used to manually count FIs that are in-focus in a single focal plane (photomicrograph). The images were taken under plane-polarized light. See Movie S1 for a full range of focal depths. (b) Methodology using secondary electron (SE) images of scanning electron microscope (SEM). (1) Take high-resolution (×4000 magnification) SE images, in which pores are darker than quartz. (2) Using ImageJ, set a threshold range to select pores or FIs (red in the processed image), and (3) postprocess the thresholded image using a combination of ‘erode’ and ‘dilate’ and modify manually the selected pores (black) by comparing to the original SE images. (4) From the processed images, measure and calculate the number and size of FIs. See the online article for the color version of this figure.

Figure 10. Sensitivity analysis to determine the minimum number of quartz grains required for calculating number density. Number densities via optical and SEM measurements are plotted against the number of grain, or cumulative increase in analysis area (panel). Note that the number density converges as the number of grain or the analysis area is increased. The number next to each point in the graphs indicates the number of panel. (a) Protomylonite sample (202)

with relatively large grains, showing increases in optical number density up to three panels. (b) Mylonite sample (201) with relatively fine grains. Based on this sensitivity analysis, more than ~15 grains are required for the representative fluid inclusion abundance of each quartz domain. Note also that fluid inclusions are mostly distributed near and along grain boundaries in the enlarged photomicrographs (left column). The top right number within parenthesis in the photomicrographs (center column) indicates distance from the shear zone core. XPL, cross-polarized light; PPL, plane-polarized light. See the online article for the color version of this figure.

Figure 11. Sensitivity analysis for 3-D heterogeneous distribution of fluid inclusions. Three samples are taken from the inner and outer mylonites and the protomylonite. The number density was optically measured from photomicrographs taken at three different focal-plane depths. See the online article for the color version of this figure.

Figure 12. Photomicrograph of another polished sample NFS2 for EBSD analysis. Red boxes are the analysis locations. The top right number within parenthesis indicates distance from the shear zone core. Rxd, recrystallized; XPL, cross-polarized light. See the online article for the color version of this figure.

Figure 13. Quartz EBSD data for micro-shear zones of sample NFS2. (a) EBSD map color-coded according to the inverse pole figure (IPF). See Fig. 12 for the location. (b) EBSD IPF map for the red box in (a). Gray lines represent subgrain boundaries. In (a) and (b), grain boundaries (black lines) and Dauphiné twin boundaries (white lines) are displayed. (c) EBSD map showing

the relative misorientation (up to 25° to reference point marked by a red cross). Black arrow corresponds to misorientation profile in (f). (d) Pole figures showing the orientation of [c], <a>, {m}, {r} and {z} for parent grain (color coded after map in (b)). All the analysis points in quartz > 20 μm are plotted. Dashed line represents the crystallographic plane of the parent quartz subparallel to the trace of the micro-shear zones. (e) Pole figures (color coded after map in (b)) and density plots of [c], <a>, {m}, {r} and {z} for recrystallized grains (one point per grain). Yellow line represents the trace of the shear zone. (f) Misorientation profile showing difference in orientation relative to the first point. (g) Misorientation angle distribution for recrystallized grains. (h) Misorientation angle/axis pairs for recrystallized grains plotted in crystal coordinates on discrete (upper) and contoured (lower) inverse pole figures with 10° intervals of misorientation except for low misorientation angles (≤10°) with 5° intervals. The locations of important crystallographic axes are marked on the first discrete plot (Lloyd, 2004). See the online article for the color version of this figure.

Figure 14. Microstructures and fluid inclusions for micro-shear zones of sample NFS2. (a) Photomicrograph of Fig. 13a with crossed polars and gypsum plate. (b) Photomicrographs for the red box in (a). Fluid inclusions along the boundaries of micro-shear zones are marked by white arrows. (c) Close-up view of a micro-shear zone (the red box in (b)). Most fluid inclusions are distributed along the boundaries of quartz grains and the micro-shear zone (marked by white arrows), and few fluid inclusions are within grains (marked by black arrow). XPL, cross-polarized light; PPL, plane-polarized light. See the online article for the color version of this figure.

Figure 15. EBSD data for highly recrystallized quartz of sample NFS2. (a) EBSD map color-coded according to the inverse pole figure (IPF). See Fig. 12 for the location. (b) EBSD IPF map for the blue box in (a). Gray lines represent subgrain boundaries. In (a) and (b), grain boundaries (black lines) and Dauphiné twin boundaries (white lines) are displayed. (c) Pole figures and density plots of [c], <a>, {m}, {r} and {z} for quartz in (b) (one point per grain). (d) Misorientation angle distribution for quartz in (b). (e) Misorientation angle/axis pairs of (b) plotted in crystal coordinates on discrete (upper) and contoured (lower) inverse pole figures with 10° intervals of misorientation except for low misorientation angles (≤10°) with 5° intervals. The locations of important crystallographic axes are marked on the first discrete plot (Lloyd, 2004). See the online article for the color version of this figure.

Figure 16. Microstructures and fluid inclusions for highly recrystallized quartz of sample NFS2. (a) Photomicrograph of Fig. 15a with crossed polars and gypsum plate. (b) Photomicrographs for the red box in (a). Fluid inclusions (FIs) are common in recrystallized quartz region but rare in parent grain. XPL, cross-polarized light; PPL, plane-polarized light. See the online article for the color version of this figure.

Figure 17. Fluid inclusion (FI) abundance with respect to perpendicular distance from the shear zone core. (a) Photomicrographs showing different number densities of FIs. The quartz domain in the second column shows the maximum FI number density of all the samples. The top right number within parenthesis indicates distance from the shear zone core. XPL, cross-polarized light; PPL, plane-polarized light. (b) Number density graph using optical measurements. (c)

Number density graph using SEM analysis. In (b) and (c), rock types and fully recrystallized (rxd) regions are also marked. See the online article for the color version of this figure.

Figure 18. Quartz domain thickness versus optical number density of fluid inclusions (FI) for samples 51 and 201 with low and high abundance, respectively. See the online article for the color version of this figure.

Figure 19. Proposed model of fluid inclusion (FI) abundance evolution during a seismic cycle in the Sandhill Corner shear zone. Before an earthquake (t_0), uniform fluid inclusion abundance is assumed across the shear zone. A co-seismic event (t_1) produces a highest abundance of FIs in the shear zone core and its continuous decrease away from the core, due to a gradient in fracture density. During post- and inter-seismic periods (t_2 and t_3), higher strain accumulation progressively removes FIs by recrystallization, with more strain (evidenced by the degree of recrystallization) and FI removal in the inner damage zone than in the outer damage zone. Consequently, a relatively large proportion of FIs survives at a distance from the core within the damage zone, causing the inter-seismic graph (t_3) of FI abundance to change slope from positive to negative. From this, a minimum width of off-fault damage zone can be estimated: from the core to the distance where the slope changes, corresponding to the peak FI abundance. See Fig. 20 for the details. See the online article for the color version of this figure.

Figure 20. Details of modeling for fluid inclusion (FI) abundance evolution during a seismic cycle. (a) Background FI abundance before earthquake. A constant distribution across the shear zone is assumed for simplicity. (b) Addition of FIs by brittle co-seismic deformation. A linearly

decreasing trend toward the shear zone boundary is used. (c) Strain or strain-rate distribution at each modeled time step during post- and inter-seismic periods. Each time step (from n_1 to n_9) after co-seismic event has an exponential decay with distance from the shear zone core. (d) Accumulated strain distribution in each time step during post- and inter-seismic periods. The accumulated strains also exhibit an exponential decrease with distance from the core. (e) Two examples of progressive removal of FIs during post- and inter-seismic periods. It is assumed that the FI removal is proportional to the accumulated strain in (d). (f) Plot of surviving FIs overlaid on (b) and (e). The post- and inter-seismic FI graphs are calculated by subtracting (e) from (b). See the online article for the color version of this figure.

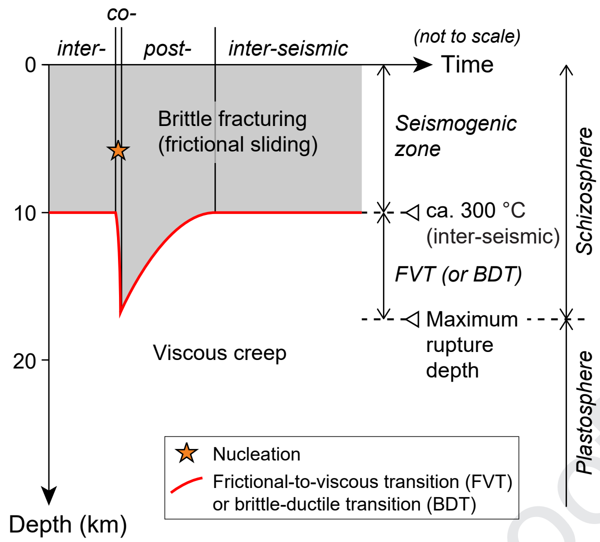
co-
inter-
post-
inter-seismic
(not to scale)
Time
0
10
20
Brittle fracturing
(frictional sliding)
Seismogenic
zone
ca. 300 °C
(inter-seismic)
FVT (or BDT)
Maximum
rupture
depth
Schizosphere
Plastosphere
Viscous creep
Nucleation
Frictional-to-viscous transition (FVT)
or brittle-ductile transition (BDT)
Depth (km)

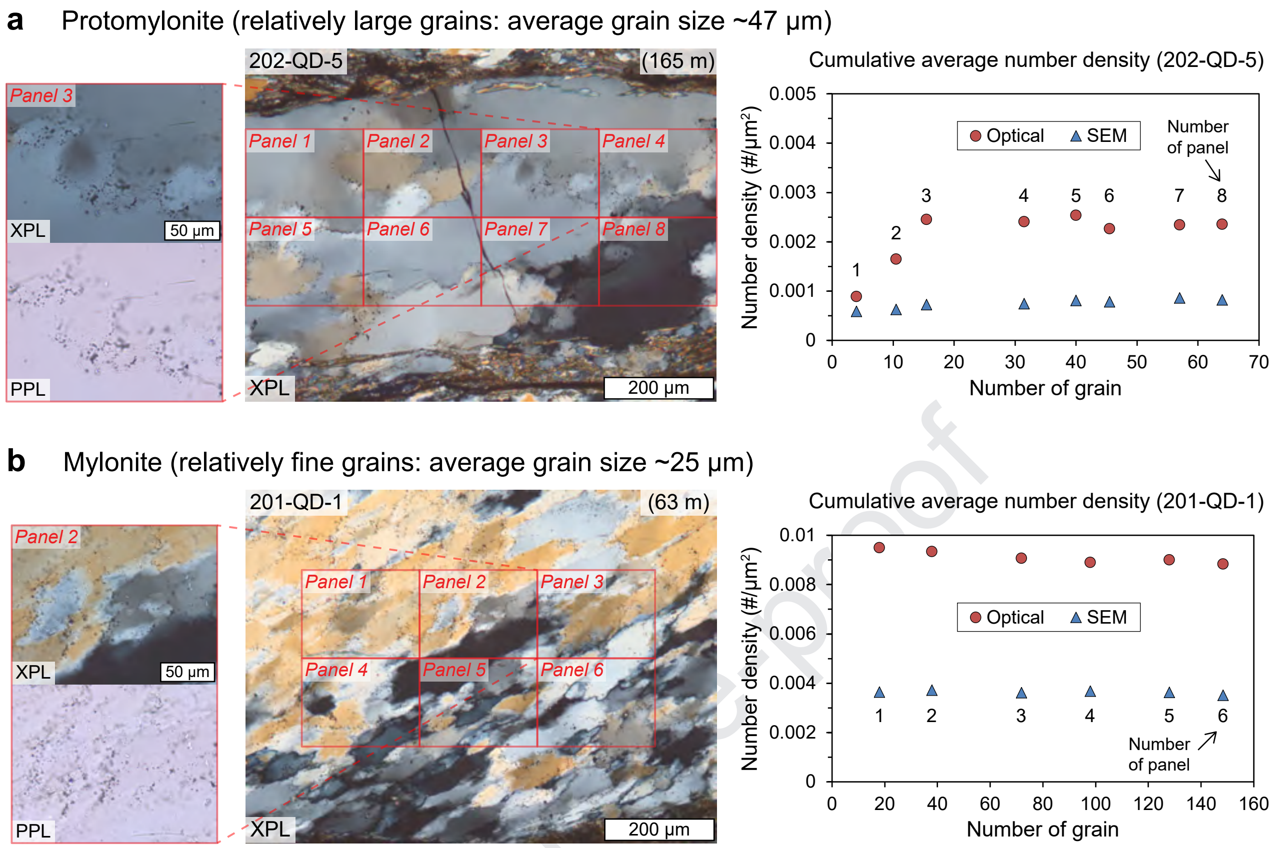
a
Protomylonite (relatively large grains: average grain size ~47 μm)
202-QD-5
(165 m)
Panel 1
Panel 2
Panel 3
Panel 4
Panel 5
Panel 6
Panel 7
Panel 8
XPL
200 μm
50 μm
PPL
Cumulative average number density (202-QD-5)
Number density (#/μm²)
Number of grain
Optical
SEM
Number of panel
b
Mylonite (relatively fine grains: average grain size ~25 μm)
201-QD-1
(63 m)
Panel 1
Panel 2
Panel 3
Panel 4
Panel 5
Panel 6
XPL
200 μm
50 μm
PPL
Cumulative average number density (201-QD-1)
Number density (#/μm²)
Number of grain
Optical
SEM
Number of panel

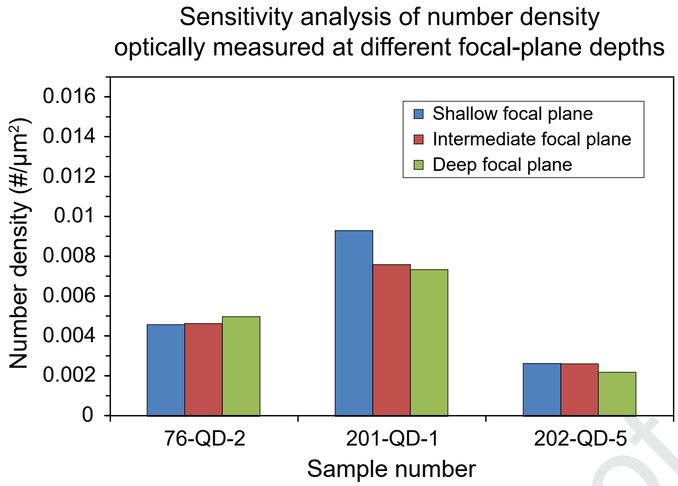
Sensitivity analysis of number density
optically measured at different focal-plane depths
Number density (#/μm²)
0.016
0.014
0.012
0.01
0.008
0.006
0.004
0.002
0
Shallow focal plane
Intermediate focal plane
Deep focal plane
76-QD-2
201-QD-1
202-QD-5
Sample number

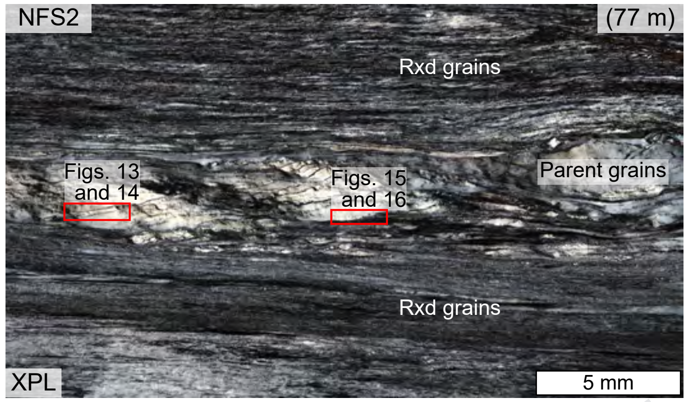
NFS2
(77 m)
Rxd grains
Figs. 13 and 14
Figs. 15 and 16
Parent grains
Rxd grains
XPL
5 mm

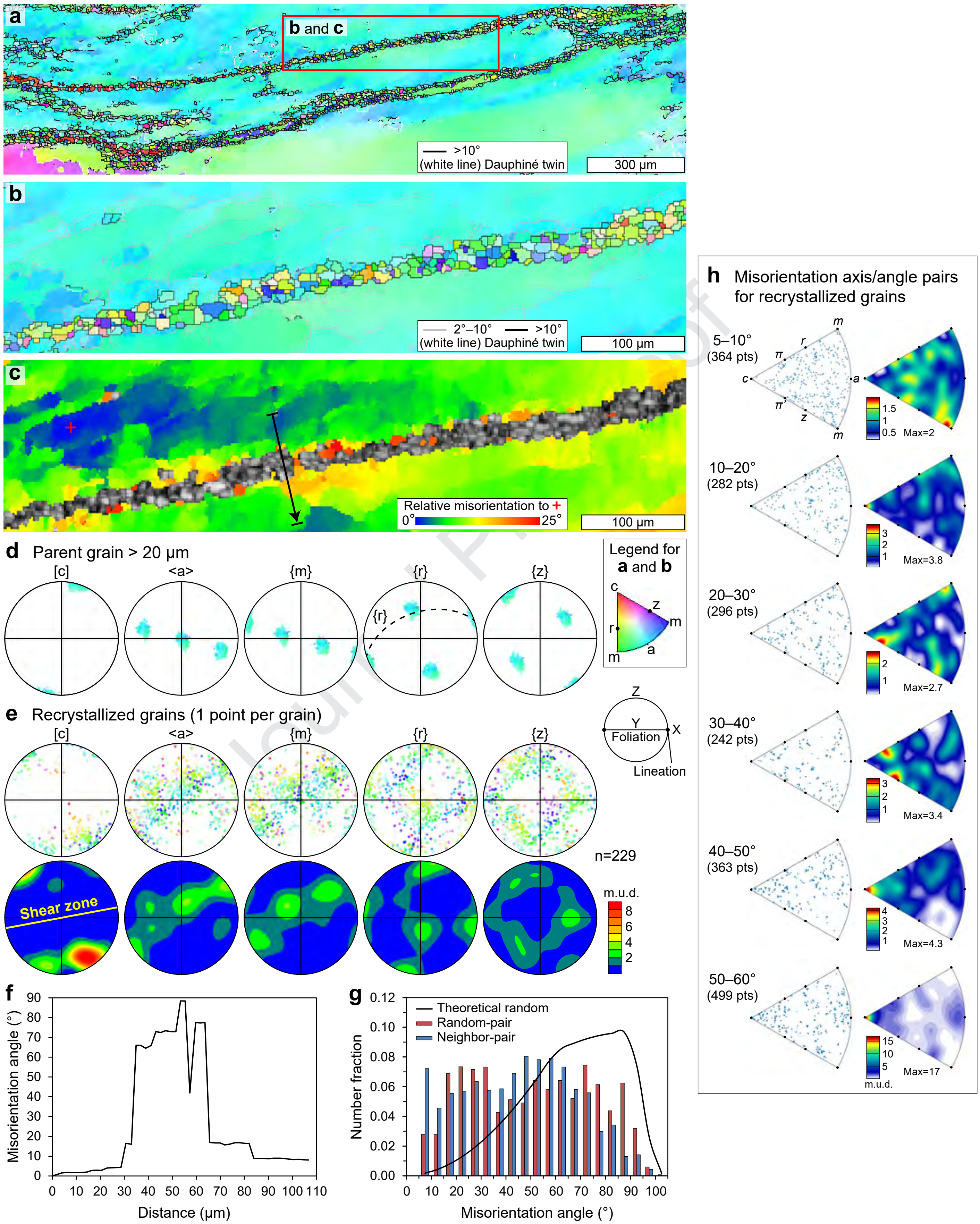
a
b and c
>10°
(white line) Dauphiné twin
300 μm
b
2°–10°
>10°
(white line) Dauphiné twin
100 μm
c
Relative misorientation to +
0°
25°
100 μm
d Parent grain > 20 μm
[c]
<a>
{m}
{r}
{z}
Legend for a and b
c
z
m
r
a
m
e Recrystallized grains (1 point per grain)
Z
Y
X
Foliation
Lineation
n=229
Shear zone
m.u.d.
8
6
4
2
f
Misorientation angle (°)
Distance (μm)
g
Number fraction
Misorientation angle (°)
Theoretical random
Random-pair
Neighbor-pair
h Misorientation axis/angle pairs for recrystallized grains
5–10° (364 pts)
Max=2
10–20° (282 pts)
Max=3.8
20–30° (296 pts)
Max=2.7
30–40° (242 pts)
Max=3.4
40–50° (363 pts)
Max=4.3
50–60° (499 pts)
Max=17
m.u.d.

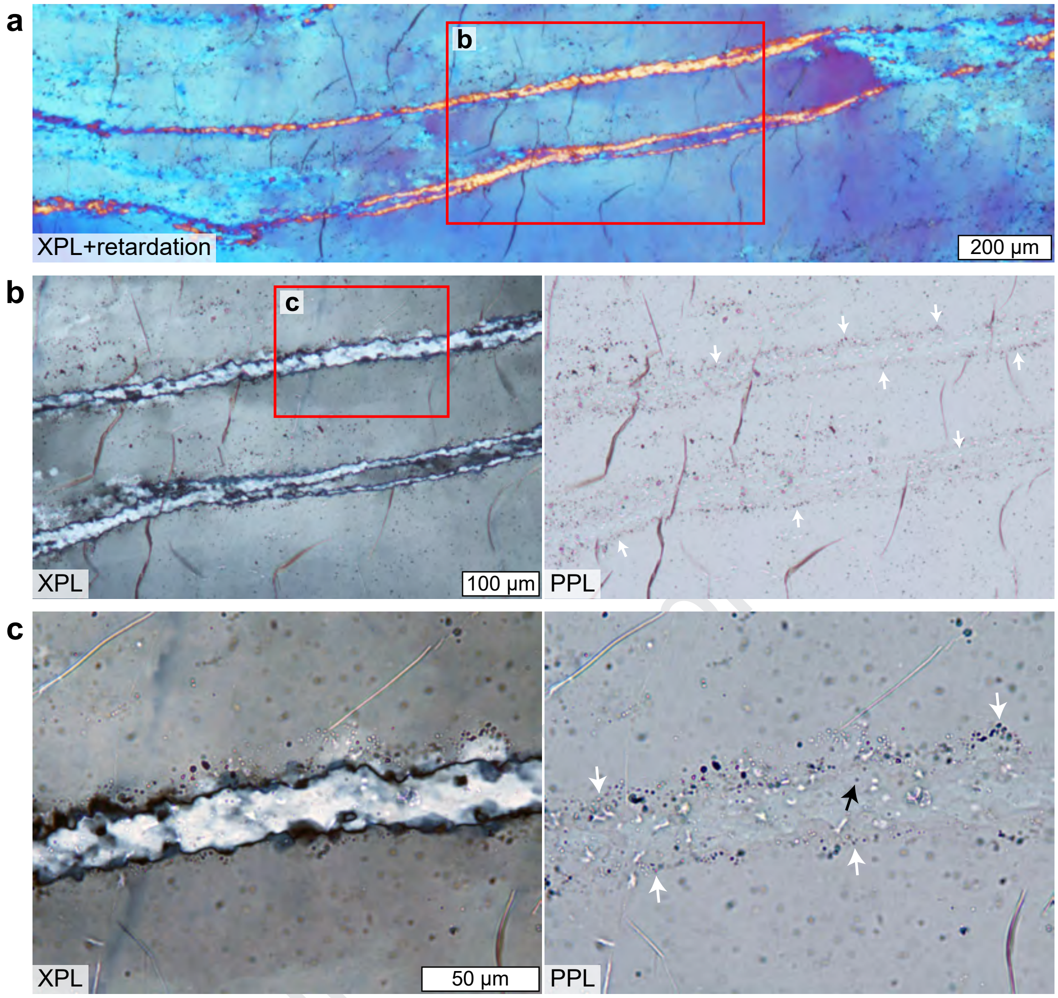
a
b
XPL+retardation
200 µm
b
c
XPL
100 µm
PPL
c
XPL
50 µm
PPL

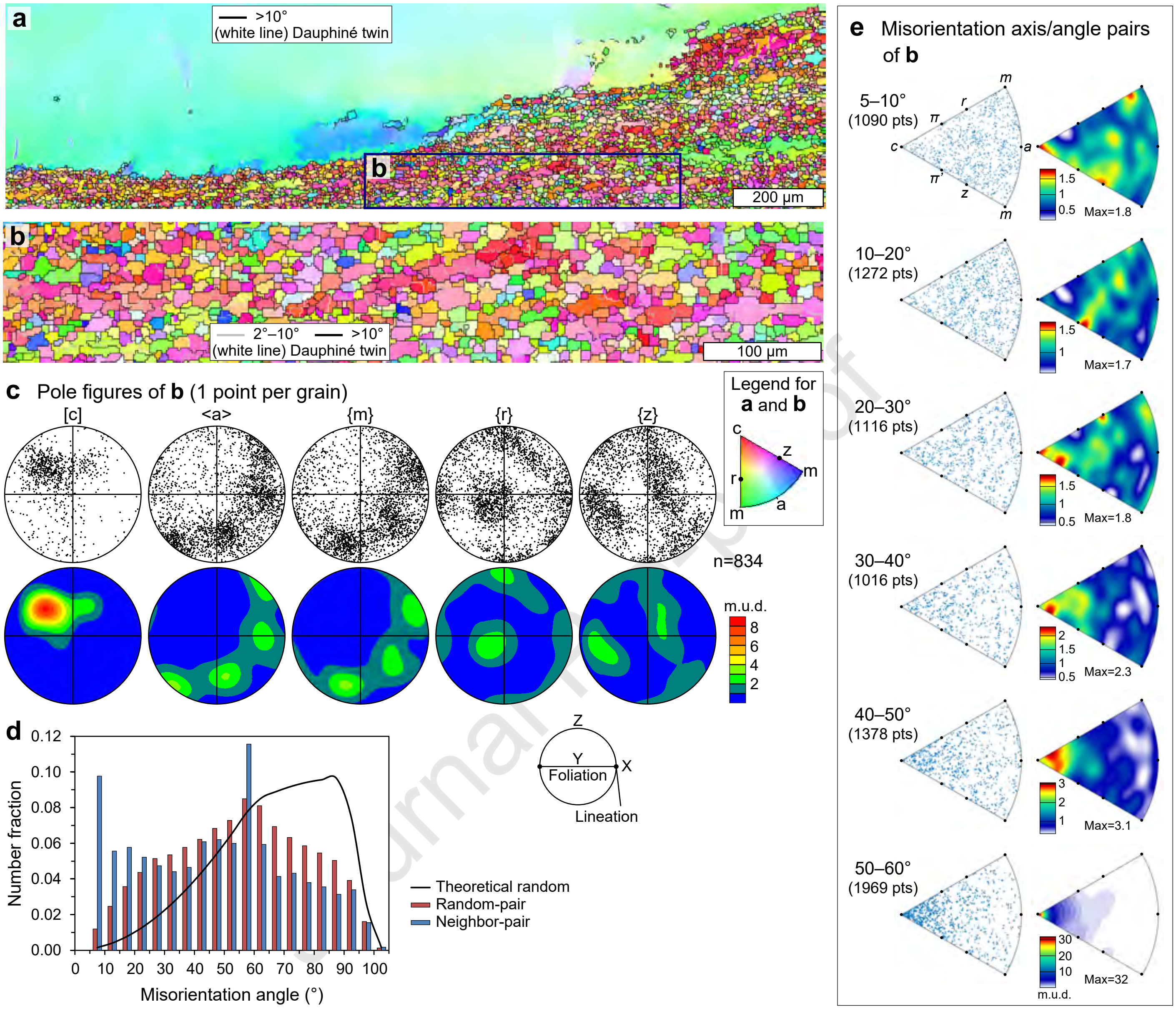
a
>10°
(white line) Dauphiné twin
200 μm
b
2°–10°
>10°
(white line) Dauphiné twin
100 μm
c Pole figures of b (1 point per grain)
[c]
<a>
{m}
{r}
{z}
Legend for a and b
n=834
m.u.d.
d
Number fraction
Misorientation angle (°)
Theoretical random
Random-pair
Neighbor-pair
Z
Y
X
Foliation
Lineation
e Misorientation axis/angle pairs of b
5–10° (1090 pts)
Max=1.8
10–20° (1272 pts)
Max=1.7
20–30° (1116 pts)
Max=1.8
30–40° (1016 pts)
Max=2.3
40–50° (1378 pts)
Max=3.1
50–60° (1969 pts)
Max=32
m.u.d.

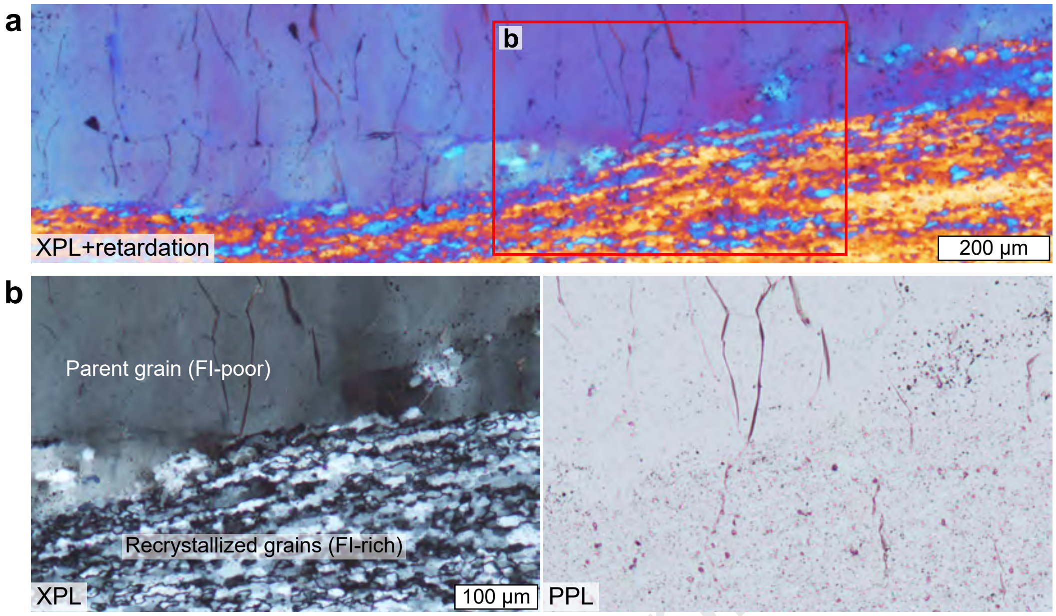
a
b
XPL+retardation
200 µm
b
Parent grain (FI-poor)
Recrystallized grains (FI-rich)
XPL
100 µm
PPL

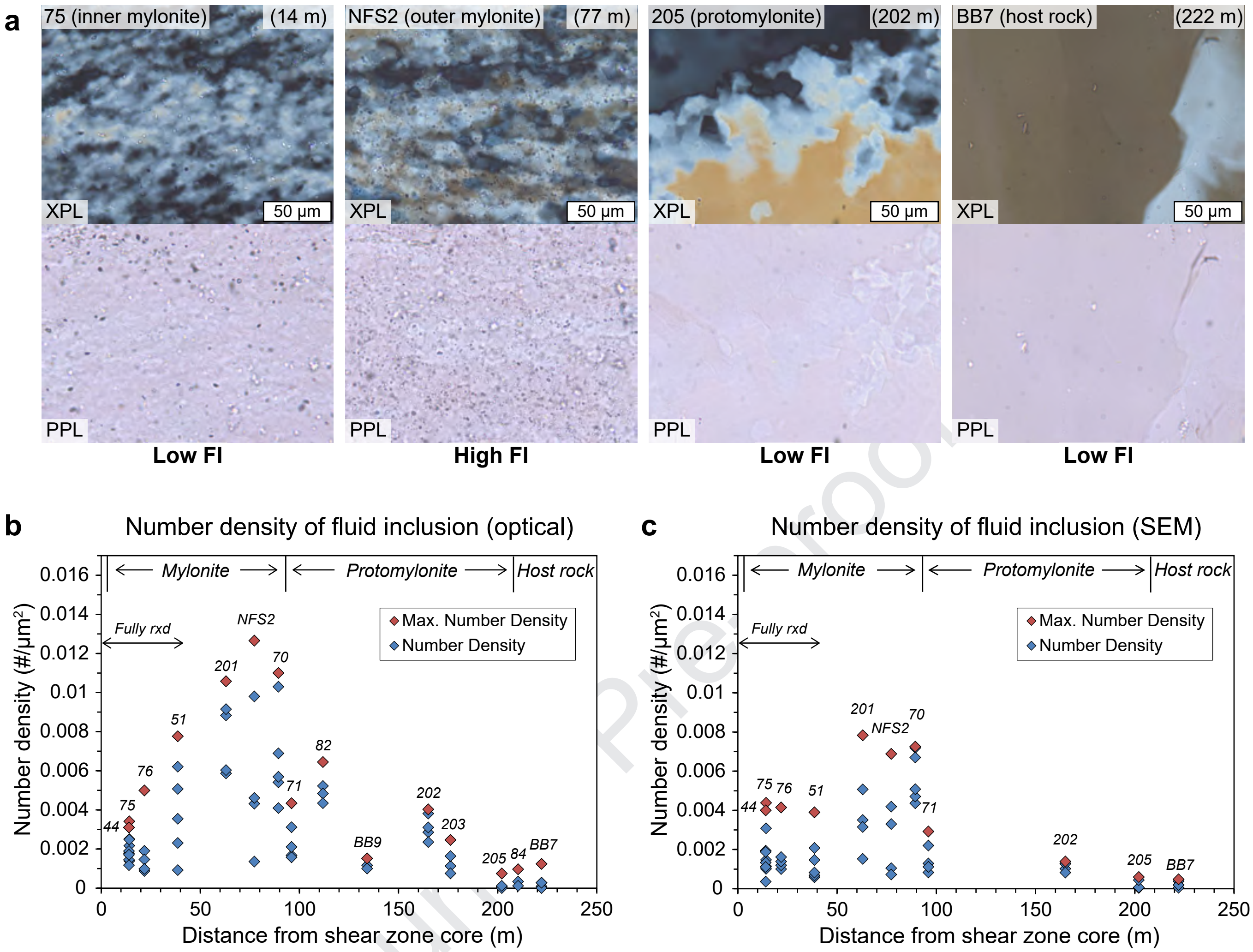
a
75 (inner mylonite)
(14 m)
NFS2 (outer mylonite)
(77 m)
205 (protomylonite)
(202 m)
BB7 (host rock)
(222 m)
XPL
50 μm
PPL
Low FI
High FI
Low FI
Low FI
b
Number density of fluid inclusion (optical)
c
Number density of fluid inclusion (SEM)
Mylonite
Protomylonite
Host rock
Fully rxd
Max. Number Density
Number Density
Number density (#/μm²)
Distance from shear zone core (m)
44
75
76
51
201
NFS2
70
71
82
BB9
202
203
205
84
BB7

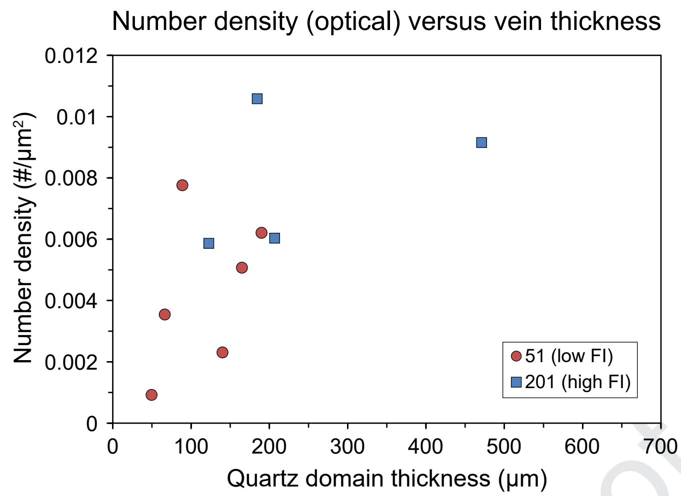
Number density (optical) versus vein thickness
Number density (#/μm²)
0.012
0.01
0.008
0.006
0.004
0.002
0
0
100
200
300
400
500
600
700
Quartz domain thickness (μm)
51 (low FI)
201 (high FI)

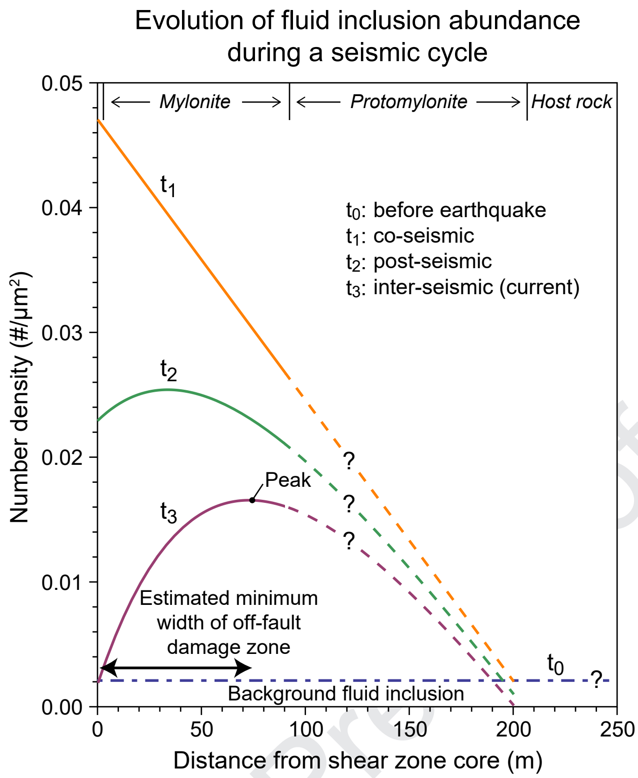

Evolution of fluid inclusion abundance during a seismic cycle
Mylonite
Protomylonite
Host rock
t0: before earthquake
t1: co-seismic
t2: post-seismic
t3: inter-seismic (current)
t1
t2
t3
Peak
?
?
?
t0
?
Estimated minimum width of off-fault damage zone
Background fluid inclusion
Number density (#/µm2)
0.00
0.01
0.02
0.03
0.04
0.05
0
50
100
150
200
250
Distance from shear zone core (m)

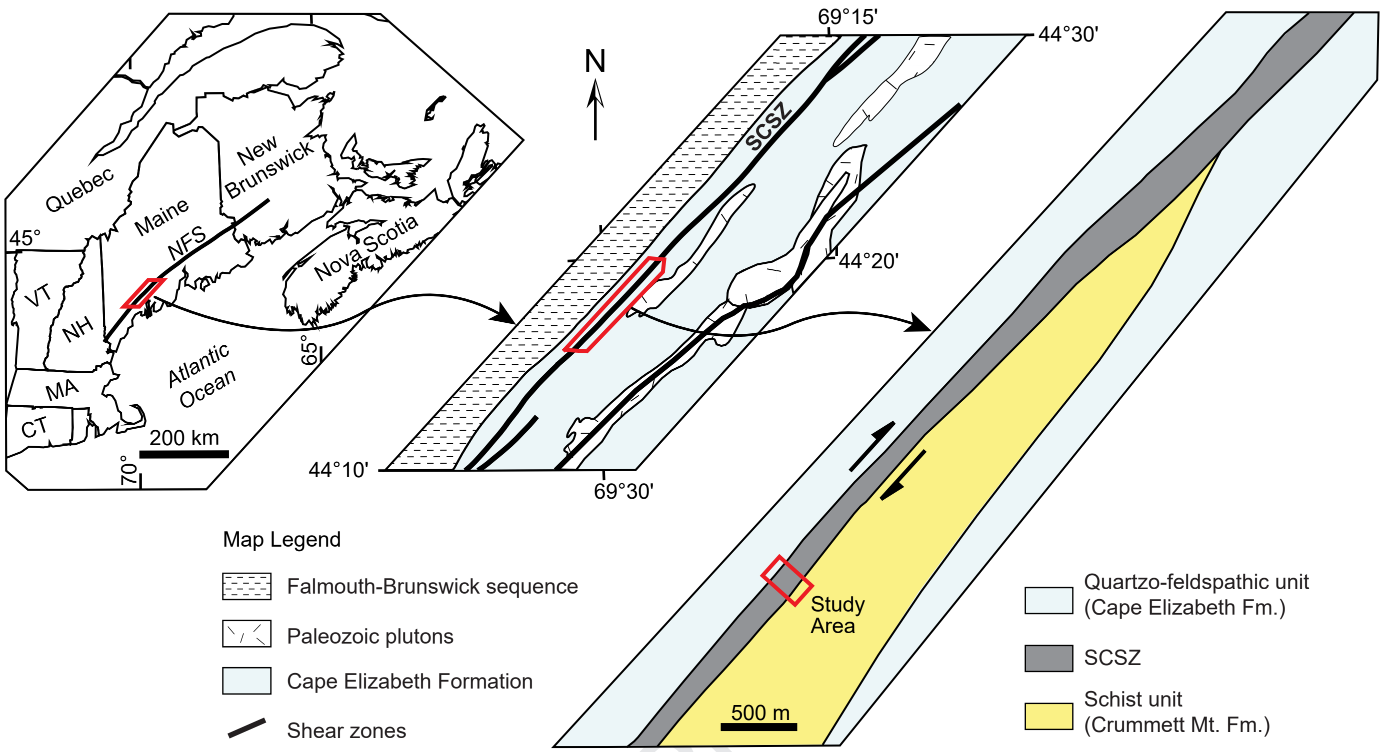

Quebec
Maine
New Brunswick
Nova Scotia
NFS
45°
VT
NH
MA
CT
Atlantic Ocean
200 km
70°
65°
N
69°15'
44°30'
SCSZ
44°20'
44°10'
69°30'
Map Legend
Falmouth-Brunswick sequence
Paleozoic plutons
Cape Elizabeth Formation
Shear zones
Study Area
500 m
Quartzo-feldspathic unit (Cape Elizabeth Fm.)
SCSZ
Schist unit (Crummett Mt. Fm.)

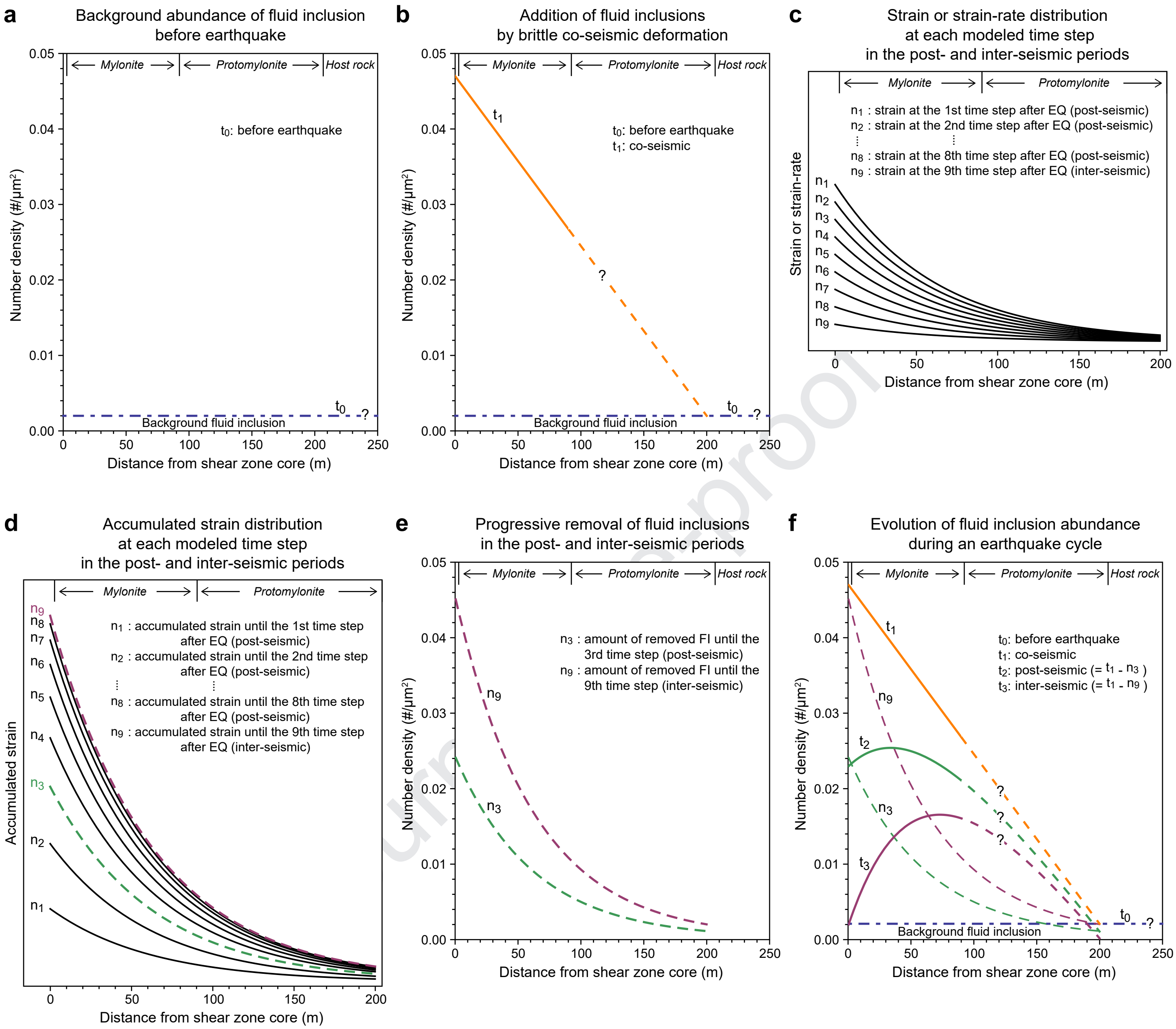
a
Background abundance of fluid inclusion before earthquake
Mylonite
Protomylonite
Host rock
t0: before earthquake
Background fluid inclusion
Number density (#/μm²)
Distance from shear zone core (m)
b
Addition of fluid inclusions by brittle co-seismic deformation
t0: before earthquake
t1: co-seismic
c
Strain or strain-rate distribution at each modeled time step in the post- and inter-seismic periods
n1 : strain at the 1st time step after EQ (post-seismic)
n2 : strain at the 2nd time step after EQ (post-seismic)
n8 : strain at the 8th time step after EQ (post-seismic)
n9 : strain at the 9th time step after EQ (inter-seismic)
Strain or strain-rate
d
Accumulated strain distribution at each modeled time step in the post- and inter-seismic periods
n1 : accumulated strain until the 1st time step after EQ (post-seismic)
n2 : accumulated strain until the 2nd time step after EQ (post-seismic)
n8 : accumulated strain until the 8th time step after EQ (post-seismic)
n9 : accumulated strain until the 9th time step after EQ (inter-seismic)
Accumulated strain
e
Progressive removal of fluid inclusions in the post- and inter-seismic periods
n3 : amount of removed FI until the 3rd time step (post-seismic)
n9 : amount of removed FI until the 9th time step (inter-seismic)
f
Evolution of fluid inclusion abundance during an earthquake cycle
t0: before earthquake
t1: co-seismic
t2: post-seismic (= t1 - n3)
t3: inter-seismic (= t1 - n9)

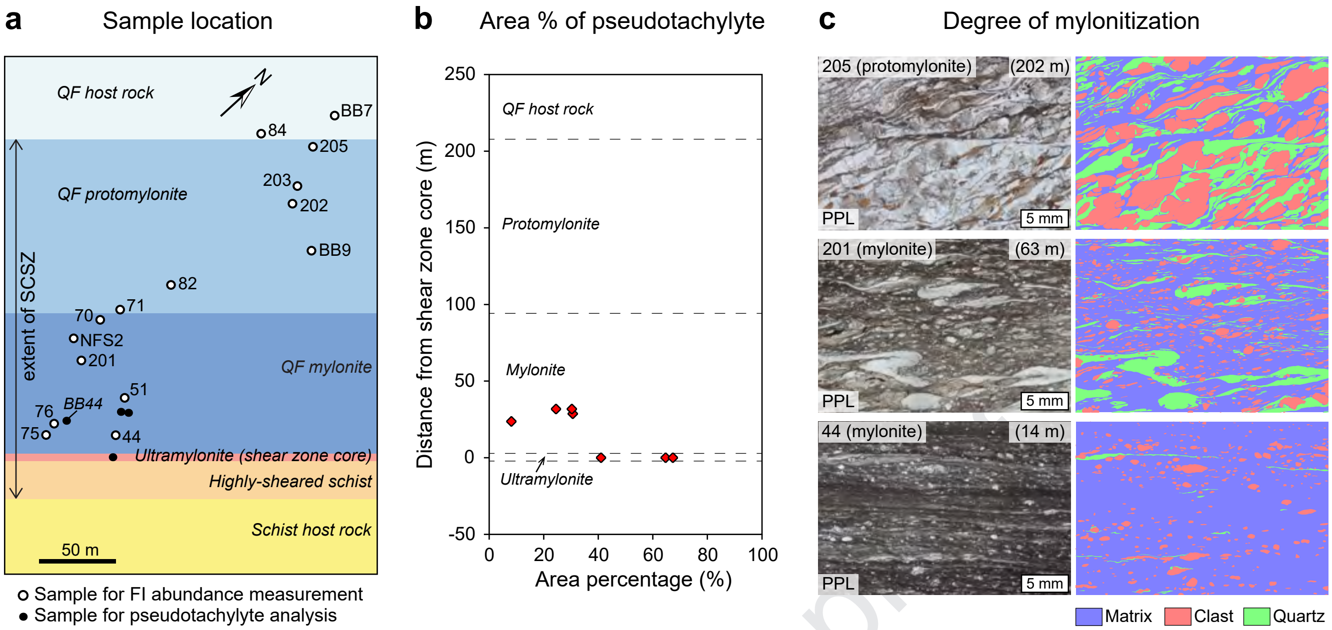
a
Sample location
QF host rock
N
BB7
84
205
203
202
QF protomylonite
BB9
82
71
70
NFS2
201
QF mylonite
extent of SCSZ
51
76
BB44
75
44
Ultramylonite (shear zone core)
Highly-sheared schist
Schist host rock
50 m
Sample for FI abundance measurement
Sample for pseudotachylyte analysis
b
Area % of pseudotachylyte
QF host rock
Protomylonite
Mylonite
Ultramylonite
Distance from shear zone core (m)
Area percentage (%)
250
200
150
100
50
0
-50
0
20
40
60
80
100
c
Degree of mylonitization
205 (protomylonite)
(202 m)
PPL
5 mm
201 (mylonite)
(63 m)
44 (mylonite)
(14 m)
Matrix
Clast
Quartz

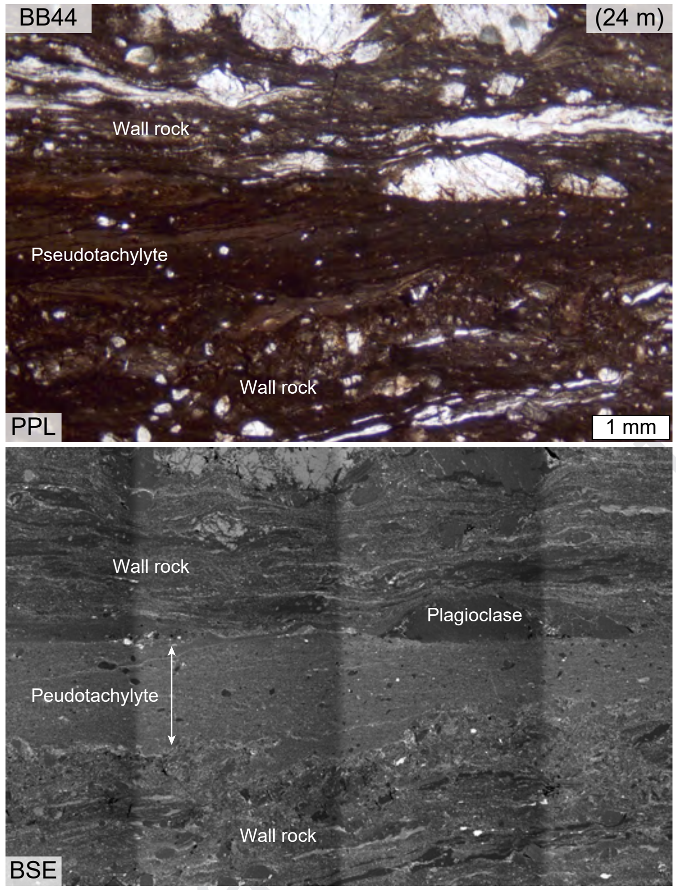
BB44
(24 m)
Wall rock
Pseudotachylyte
Wall rock
PPL
1 mm
Wall rock
Plagioclase
Peudotachylyte
Wall rock
BSE

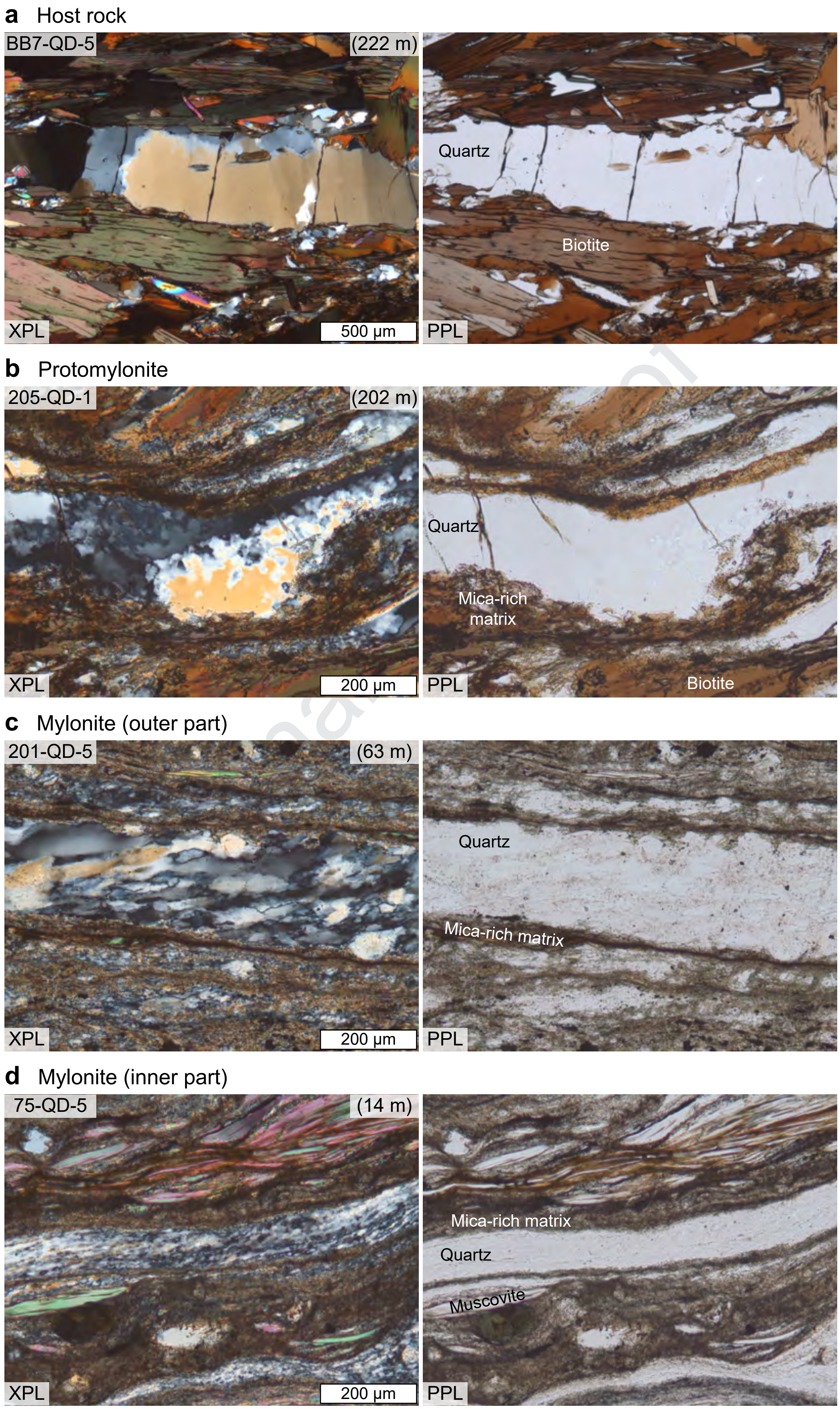
a Host rock
BB7-QD-5
(222 m)
Quartz
Biotite
XPL
500 µm
PPL
b Protomylonite
205-QD-1
(202 m)
Quartz
Mica-rich matrix
Biotite
XPL
200 µm
PPL
c Mylonite (outer part)
201-QD-5
(63 m)
Quartz
Mica-rich matrix
XPL
200 µm
PPL
d Mylonite (inner part)
75-QD-5
(14 m)
Mica-rich matrix
Quartz
Muscovite
XPL
200 µm
PPL

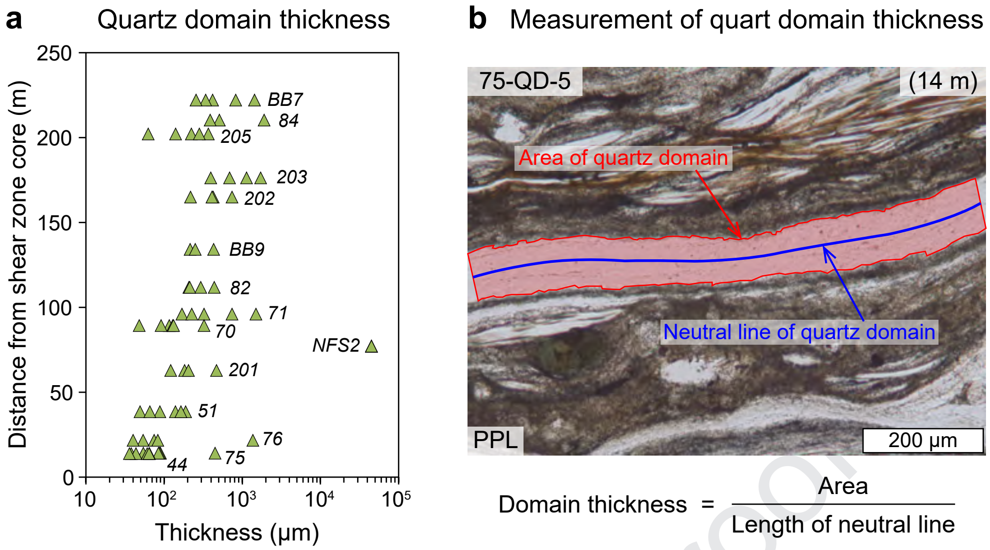

$$\text{Domain thickness} = \frac{\text{Area}}{\text{Length of neutral line}}$$

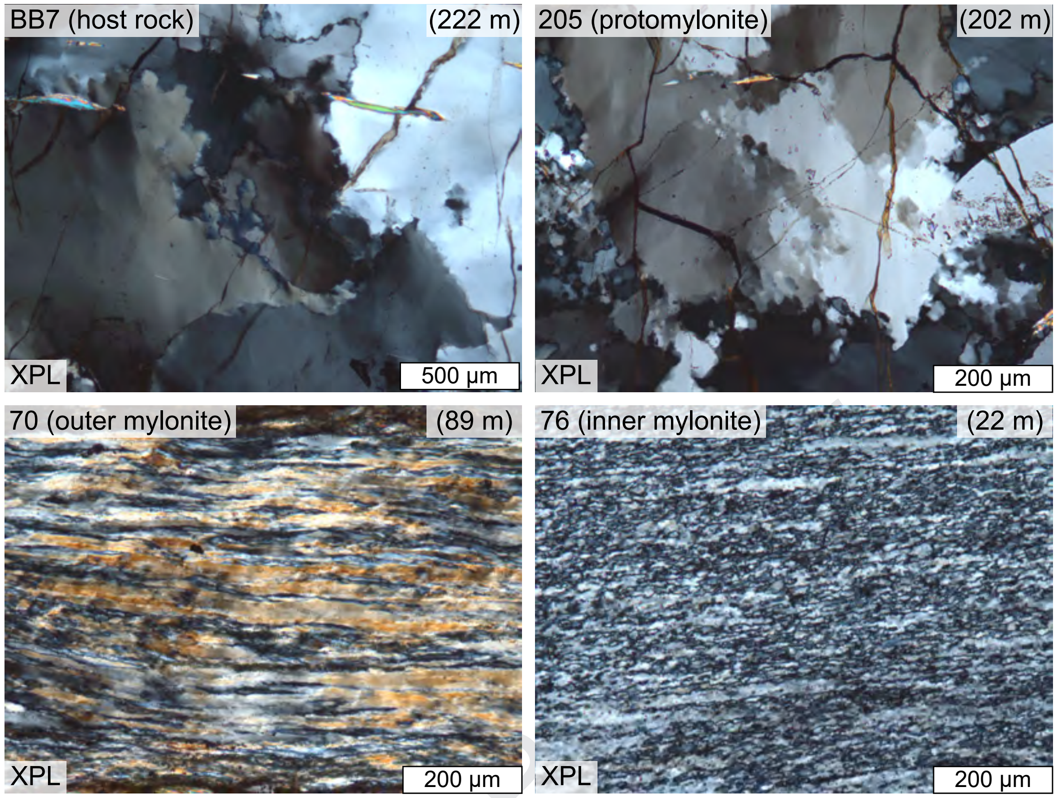
BB7 (host rock)
(222 m)
XPL
500 μm
205 (protomylonite)
(202 m)
XPL
200 μm
70 (outer mylonite)
(89 m)
XPL
200 μm
76 (inner mylonite)
(22 m)
XPL
200 μm

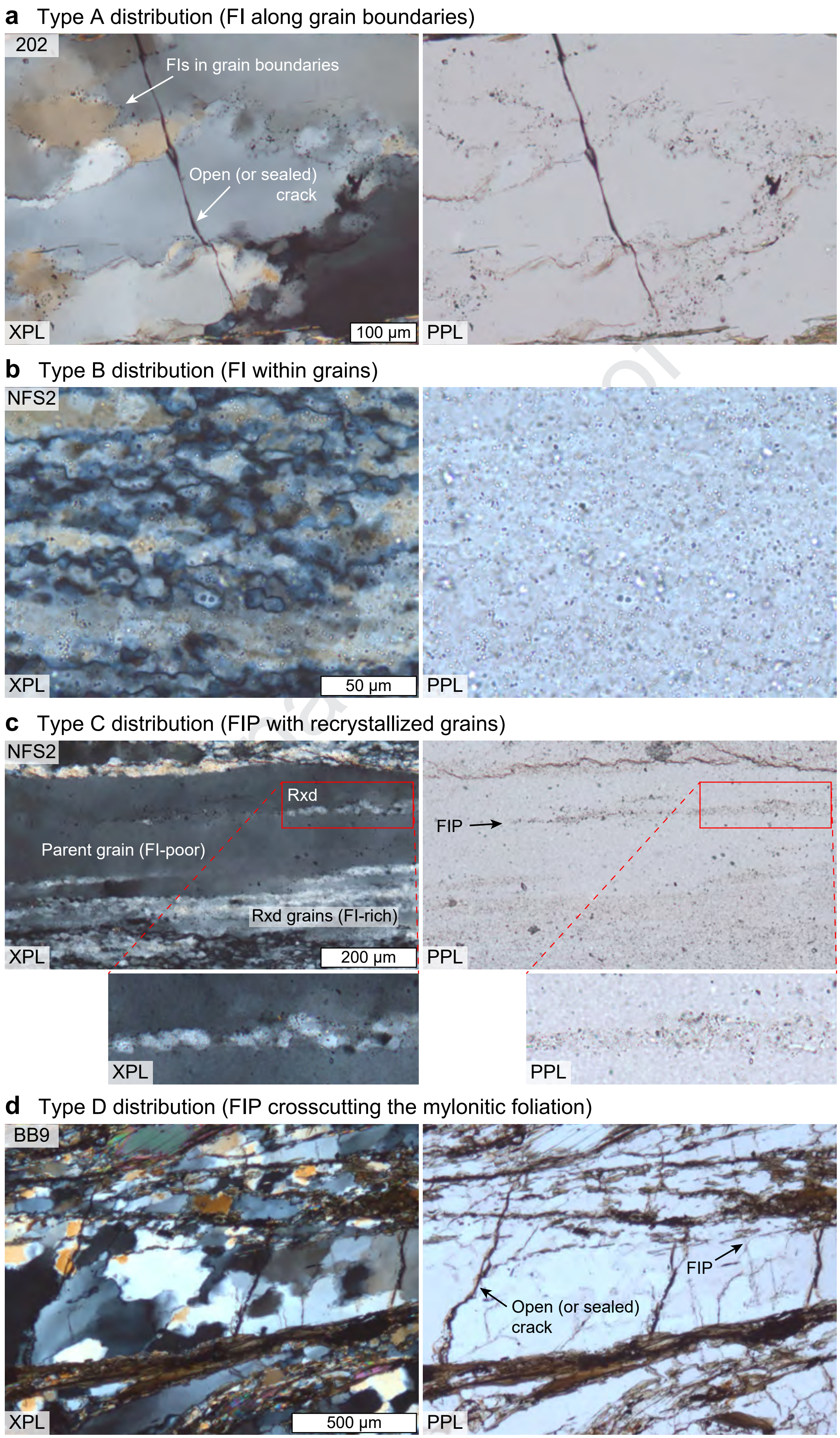
a Type A distribution (FI along grain boundaries)
202
FIs in grain boundaries
Open (or sealed) crack
XPL
100 μm
PPL
b Type B distribution (FI within grains)
NFS2
XPL
50 μm
PPL
c Type C distribution (FIP with recrystallized grains)
NFS2
Rxd
Parent grain (FI-poor)
Rxd grains (FI-rich)
FIP
XPL
200 μm
PPL
XPL
PPL
d Type D distribution (FIP crosscutting the mylonitic foliation)
BB9
FIP
Open (or sealed) crack
XPL
500 μm
PPL

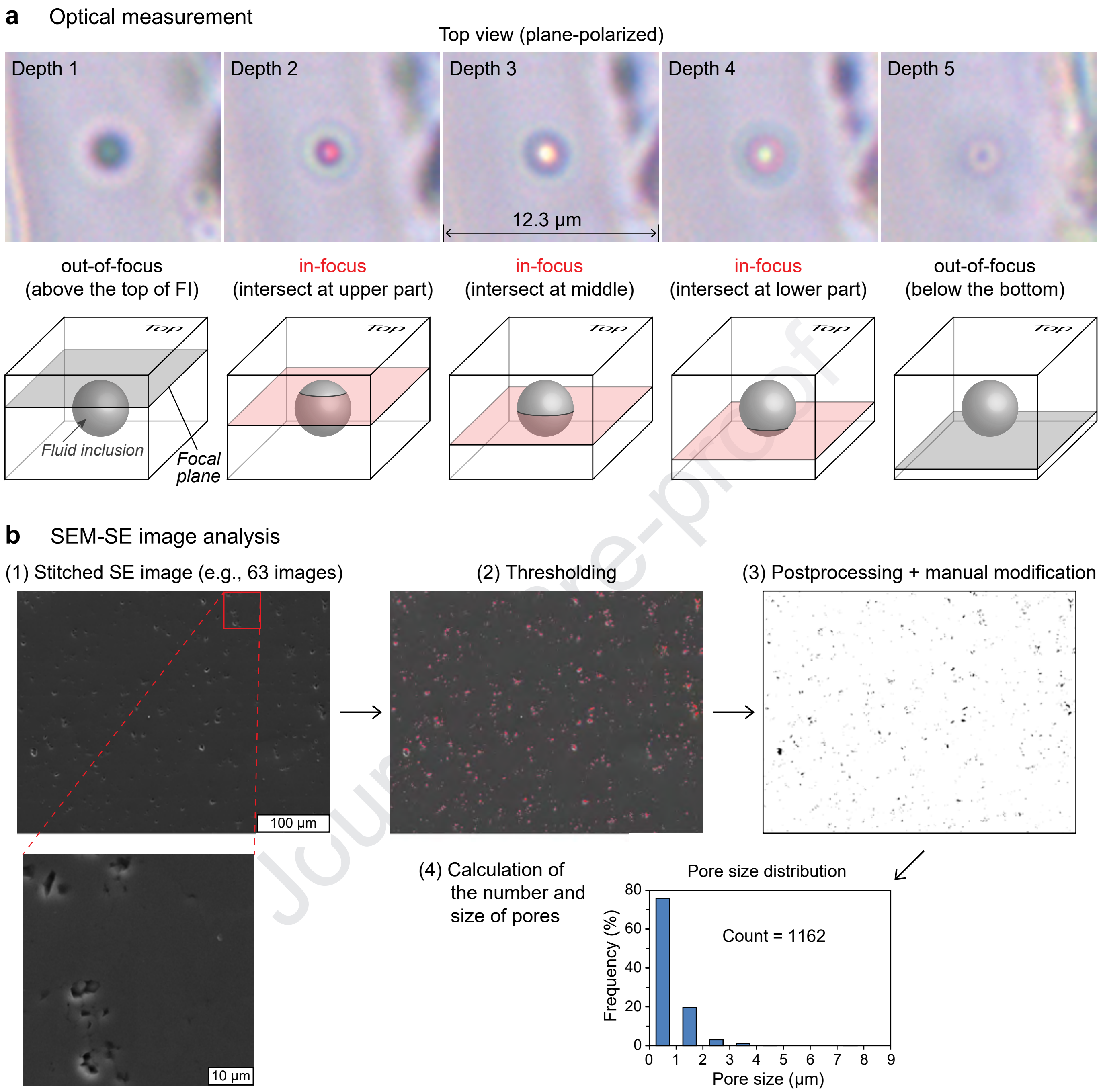
a
Optical measurement
Top view (plane-polarized)
Depth 1
Depth 2
Depth 3
Depth 4
Depth 5
12.3 μm
out-of-focus
(above the top of FI)
in-focus
(intersect at upper part)
in-focus
(intersect at middle)
in-focus
(intersect at lower part)
out-of-focus
(below the bottom)
Top
Fluid inclusion
Focal plane
b
SEM-SE image analysis
(1) Stitched SE image (e.g., 63 images)
(2) Thresholding
(3) Postprocessing + manual modification
100 μm
10 μm
(4) Calculation of the number and size of pores
Pore size distribution
Count = 1162
Frequency (%)
Pore size (μm)
0
20
40
60
80
1
2
3
4
5
6
7
8
9

Highlights

- Quartz records co-seismic damage in a mid-crustal strike-slip fault/shear zone
- Fluid-inclusion abundance shows a low-high-low trend from the shear zone core
- Fluid-inclusion abundance is reduced by post- and inter-seismic recrystallization
- Reduction of fluid-inclusion abundance is greatest in the inner shear zone
- The off-fault damage zone is >~80 m wide at frictional-to-viscous transition depths

Declaration of interests

☒ The authors declare that they have no known competing financial interests or personal relationships that could have appeared to influence the work reported in this paper.

☐The authors declare the following financial interests/personal relationships which may be considered as potential competing interests: